

CONSTRAINING MARS OBLIQUITY HISTORY IN THE AMAZONIAN AND HESPERIAN PERIODS USING ELLIPTIC CRATER ORIENTATIONS

BY

JAMES YUNZHANG HU

AN HONORS THESIS SUBMITTED TO
THE DEPARTMENT OF THE GEOPHYSICAL SCIENCES
IN PARTIAL FULFILLMENT OF THE REQUIREMENTS FOR
THE DEGREE OF BACHELOR OF SCIENCE WITH HONORS

THE COLLEGE OF THE UNIVERSITY OF CHICAGO

THESIS ADVISER: EDWIN S. KITE

SECOND READER: DORIAN S. ABBOT

CHICAGO, ILLINOIS, U.S.A.

MAY 2022

14

15

To waipo

TABLE OF CONTENTS

17	LIST OF FIGURES	v
18	LIST OF TABLES	vi
19	ACKNOWLEDGMENTS	vii
20	ABSTRACT	viii
21	1 INTRODUCTION	1
22	1.1 Theoretical background on Mars obliquity variation	1
23	1.2 A brief history of Mars obliquity reconstruction	2
24	1.3 Relevance and indirect evidence of Mars obliquity variation	3
25	1.4 Geologic constraints on historical Mars obliquity	4
26	1.5 Overview of this study	6
27	2 METHODS	7
28	2.1 Overview of methods	7
29	2.2 Collection of crater azimuth data	7
30	2.3 Adaptation of Holo et al. (2018)'s forward model	12
31	2.4 Determination of best-fit obliquity and geologic unit age	13
32	2.5 Sensitivity checks	17
33	3 RESULTS	18
34	3.1 Simulated and observed crater azimuth distributions	18
35	3.2 Simulated–observed crater azimuth distribution comparisons	18
36	3.3 Mean obliquity of Mars over geologic time	18
37	4 DISCUSSION	22
38	4.1 Synthesis of results	22
39	4.2 Comparison with previous studies	23
40	4.3 Sensitivity tests	25
41	4.4 Implications of results	29
42	4.5 Limitations of this study	30
43	5 CONCLUSION	33
44	REFERENCES	35
45	APPENDIX: CODE	42
46	A.1 hu_01_get_crater_data.m	42
47	A.2 hu_02_get_azimuth_diffs.m	45
48	A.3 hu_03_get_pois.m	47
49	A.4 hu_04_apply_obliquity.m	52

50	A.5 hu_05_apply_lat_dist.m	55
51	A.6 hu_06_get_mismatch.m	59
52	A.7 hu_07_plot_age_obliquity.m	72
53	A.8 hu_08_perturb_data_iaerr.m	80
54	A.9 hu_09_get_mismatch_var_ecrit.m	82
55	A.10 hu_10_plot_distributions.m	91

LIST OF FIGURES

57	2.1	Flow chart overview of this study's methods	8
58	2.2	Tanaka et al. (2014) geologic map of Mars, with sampled areas outlined	9
59	2.3	Two sampled craters in the AHv unit	10
60	2.4	Distribution of traced crater ellipticities	11
61	2.5	Physical basis for variation in elliptic crater azimuth distribution	14
62	2.6	Schematic representation of the impact simulation model	15
63	3.1	Distribution of simulated and observed crater azimuths	19
64	3.2	Mismatch between the simulated and observed crater azimuth distributions . . .	20
65	3.3	Mean obliquity of Mars over time (logarithmic scale)	21
66	4.1	Latitude frequency histogram of traced craters	23
67	4.2	Distribution of observed crater azimuths by ellipticity threshold	27
68	4.3	Simulated–observed crater azimuth distribution mismatch by ellipticity threshold	28
69	4.4	Azimuth frequency histogram of traced craters	32

LIST OF TABLES

71	3.1	Summary of simulated–observed mismatch results for crater azimuth distribution	18
72	3.2	Absolute ages of sampled geologic units.	19
73	4.1	Inter-analyst variability in traced elliptic crater azimuths.	26
74	4.2	Simulated–observed crater azimuth distribution mismatch by threshold ellipticity	27

ACKNOWLEDGMENTS

76 I would like to thank my adviser Edwin Kite, without whom this project would not be
77 possible, for his ideas, knowledge, guidance, and direction throughout this yearlong endeavor
78 during which I have learned so much about Mars and planetary science. I'm also grateful to
79 Dorian Abbot for his constructive comments and insights.

80 I'd also like to thank my program instructors and colleagues at the Marine Biological
81 Laboratory in Woods Hole for condoning mid-lecture crater-tracing (and for giving me a
82 great first taste of original scientific research). Thanks especially to Alice Ball for our thesis
83 focus sessions.

84 Thank you to mum and dad for buying every space and dinosaur encyclopedia little me
85 ever wanted and, more recently, listening to me ramble about Holo et al. (2018). Thank you
86 to my dearly missed *waipo*, to whom this thesis is dedicated. Thank you to Puyu Shi for her
87 constant love and support.

ABSTRACT

Mars's past obliquity governs many aspects of its past climate, including its surface volatile dynamics, atmospheric collapse, and low-latitude ice migration. Yet because Mars obliquity oscillates chaotically over >100 Ma time scales, the bulk of Mars's past obliquity cannot be determined through physical simulations and is therefore unknown. This study attempts to constrain Mars's past obliquity by adapting a recently developed statistical technique that compares the orientations (azimuths) of actually observed elliptic craters to those of simulated craters under different obliquity scenarios in which Mars obliquity was held constant over the simulated time period. To obtain the azimuths of actually observed elliptic craters, we traced 1,678 elliptic craters collectively from the late Amazonian volcanic (lAv) and Amazonian–Hesperian volcanic (AHv); separately, we simulated 10^6 craters per constant-obliquity scenario for each geologic unit. We compared then the actual and simulated craters' respective azimuth distributions with the azimuth distributions, measuring the extent of simulation–data mismatch by conducting χ^2 tests whereby the best-fit obliquity scenarios were those yielding the smallest reduced χ^2 statistic, for each geologic unit. We found that the mean obliquities associated with the lAv unit, representing the past ~ 0.9 Ga, and AHv unit, representing the past ~ 2.0 Ga, were 66° (56.2° – 74.6° standard deviation interval) and 8° (0.0° – 14.4° standard deviation interval), respectively. As a sensitivity test, we quantified the inter-analyst tracing error on azimuth measurements and applied those errors at random to our crater azimuths 1,000 times, thus generating 1,000 new sets of 1,678 inter-analyst-perturbed crater azimuths. We found (in our median inter-analyst-perturbed result) that the mean obliquities associated with the lAv and AHv units were 63° (54.7° – 72.0° standard deviation interval) and 14° (6.3° – 20.5° standard deviation interval), respectively. These results' geologic implications include that, relative to today ($\sim 25^\circ$ obliquity), Mars saw, over the past ~ 2.0 Ga, more intense polar glaciation, polar atmospheric collapse, and desiccation of deep aquifers and saw, over the past ~ 0.9 Ga, greater sublimation of water ice, the mi-

¹¹⁴ gration to lower latitudes of water ice, higher water vapor pressure, and more frequent polar
¹¹⁵ dust storms. Future work may collect a larger set of craters, apply this study's methods
¹¹⁶ to Holo et al. (2018)'s dataset and vice versa, account for poke-throughs of older craters
¹¹⁷ on younger terrain, and investigate why our method implies an unphysical result for the
¹¹⁸ intervening \sim 1.0 Ga period between the ages of the units.

119

1 INTRODUCTION

120 1.1 Theoretical background on Mars obliquity variation

121 Currently at $\sim 25^\circ$, Mars obliquity, or the tilt of its polar axis relative to the normal to its
122 orbital plane, has varied dramatically over geologic time, primarily because of gravitational
123 forcing by Jupiter (Laskar et al., 2004). The obliquity evolution of post-Noachian Mars is
124 of great interest as it has strongly affected its climate, atmosphere, hydrology, and surface
125 features; accurate reconstructions of Mars obliquity history are critical to the study of the
126 planet's paleoclimates and past habitability (Ward, 1973; Jakosky & Carr, 1985; Laskar
127 et al., 2004).

128 Through the reverse integration of Mars's orbital and rotational equations, reconstruction
129 efforts have identified significant obliquity variations on both periodic and secular timescales
130 (Ward, 1973; Touma & Wisdom, 1993; Laskar & Robutel, 1993; Laskar et al., 2004). The
131 obliquity of Mars presently oscillates between $\sim 15^\circ$ and $\sim 35^\circ$ within periods of ~ 100 ka–
132 1 Ma (in stark contrast to Earth's Moon-stabilized obliquity, which stays within $\pm 1.3^\circ$ of
133 the mean value), although over the past ~ 300 ka the amplitude has temporarily decreased
134 to just a few degrees from the mean (Laskar et al., 2004). The past obliquity of Mars is
135 precisely characterized to ~ 20 Ma ago, when it oscillated around a mean of $\sim 35^\circ$ before
136 abruptly transitioning to the present range at ~ 5 Ma ago (Laskar et al., 2004, 2010).

137 Beyond ~ 100 Ma ago, however, chaotic diffusion dominates, because the moments of
138 inertia of Mars can change such that the planet encounters secular spin-orbit resonances—
139 events wherein the period of spin axis precession matches a period in the variation of Mars's
140 orbital plane inclination—that, in turn, cause large, unpredictable swings in obliquity (Ward
141 et al., 1979). Consequently, obliquity may have wandered between 0° and $\sim 70^\circ$, such that
142 the bulk of Mars obliquity history since Solar System formation cannot be exactly recovered
143 through numerical integration (Touma & Wisdom, 1993; Laskar & Robutel, 1993; Laskar

¹⁴⁴ et al., 2004). To characterize Mars obliquity history beyond the geologically recent past,
¹⁴⁵ today's researchers have therefore been forced to eschew numerical integration in favor of
¹⁴⁶ statistical analysis and surface observation (e.g., Laskar et al., 2004; Holo et al., 2018).

¹⁴⁷ 1.2 A brief history of Mars obliquity reconstruction

¹⁴⁸ As summarized by Laskar et al. (2004), Mars researchers initially placed their focus on the
¹⁴⁹ precession of the planet's axis and the evolution of its eccentricity (Leighton & Murray, 1966;
¹⁵⁰ Murray et al., 1973). Applying the same lens as those who pointed out that Earth's $\pm 1.3^\circ$
¹⁵¹ oscillations in obliquity have significantly shaped its paleoclimate, Ward (1973) calculated
¹⁵² that Mars had experienced $\pm \sim 10^\circ$ oscillations and concluding that resolving past obliquity
¹⁵³ forcing would be indispensable to the understanding of features including its paleoclimate,
¹⁵⁴ paleohydrology, and surface geology. In parallel, advancements in computing technology,
¹⁵⁵ astronomical calculation, and space exploration successively improved researchers' ability to
¹⁵⁶ constrain the recent (past ~ 100 Ma) obliquity history of Mars (e.g., Brouwer & van Woerkom,
¹⁵⁷ 1950; Bretagnon, 1974; Laskar, 1988; Folkner et al., 1997; Yoder & Standish, 1997).

¹⁵⁸ By far the most significant advancements in the understanding of Mars obliquity varia-
¹⁵⁹ tion, however, have not been the refinement of deterministic reverse integrations. It was orig-
¹⁶⁰ inally thought that, even on ~ 1 Ga timescales, obliquity non-chaotically oscillated around
¹⁶¹ $\sim 25^\circ$ in the post-Noachian period (Ward, 1974, 1979, 1992). Separately by Touma & Wis-
¹⁶² dom (1993) and by Laskar & Robutel (1993), it was proposed that chaotic secular spin-orbit
¹⁶³ resonances pose an insurmountable barrier to the numerical solution of >100 Ma ago Mars
¹⁶⁴ obliquity. Laskar et al. (2004) later reinforced this result by statistically demonstrating that,
¹⁶⁵ based on a large number of obliquity solutions and orbital solutions, chaotic diffusion domi-
¹⁶⁶ nates the planet's obliquity evolution over secular timescales. Bills & Keane (2019) posited,
¹⁶⁷ in dissent, that obliquity variations are likely non-chaotic because small magnitudes of en-
¹⁶⁸ ergy dissipation can dampen chaotic variations, and moreover that obliquity variations are

¹⁶⁹ fully damped such that future variations can be computed; yet even they agree that past
¹⁷⁰ obliquity oscillations (except the past mean obliquity) cannot be accessed.

¹⁷¹ 1.3 Relevance and indirect evidence of Mars obliquity variation

¹⁷² Past obliquity oscillations are particularly relevant to the history of surface volatiles, espe-
¹⁷³ cially water and CO₂, on Mars (reviewed in Jakosky, 2021). A primary mechanism through
¹⁷⁴ which obliquity modifies Martian climate is by controlling the summer insolation on polar
¹⁷⁵ ice caps, which are composed of both water ice and dry (CO₂) ice. Whereas the poles are
¹⁷⁶ well shielded from the Sun at low obliquity, they experience intense summer insolation at
¹⁷⁷ high obliquity. In the former case, colder poles thin out the atmosphere by precipitating
¹⁷⁸ gaseous CO₂, thus driving the collapse of the Martian atmosphere at the poles (Lindner &
¹⁷⁹ Jakosky, 1985; Kreslavsky & Head, 2005; Phillips et al., 2011; Soto et al., 2015). In the latter
¹⁸⁰ case, polar water ice undergoes enhanced sublimation, both migrating to lower latitudes and
¹⁸¹ increasing the pressure of water vapor (Haberle & Jakosky, 1990; Jakosky et al., 1995; Zent,
¹⁸² 2013; Forget et al., 2017). Further consequences of dramatic obliquity excursions relate to
¹⁸³ dust storms, more likely to initiate near poles at high obliquity, and deep aquifers, more likely
¹⁸⁴ to desiccate via sublimation at low obliquity (Haberle et al., 2003; Grimm et al., 2017).

¹⁸⁵ Indirect evidence of past obliquity oscillation is present in various forms. Although water
¹⁸⁶ ice is presently unstable below polar latitudes on present-day Mars, there exists extensive
¹⁸⁷ evidence of mid- and low-latitude debris-covered glaciers, which likely formed due to the
¹⁸⁸ migration of polar ice in periods of high obliquity (Head et al., 2003; Dickson et al., 2008;
¹⁸⁹ Adeli et al., 2019). Geomorphic features like mid-latitude smooth mantled deposits and
¹⁹⁰ glacial deposits on the northwestern flanks of Tharsis Montes further suggest water ice was
¹⁹¹ deposited below polar latitudes, likely during high obliquity (Mustard et al., 2001; Head &
¹⁹² Marchant, 2003; Head et al., 2003; Milkovich et al., 2006; Shean et al., 2007). The formation of
¹⁹³ mid-latitude and tropical glaciers during past ice ages were also likely significantly controlled

¹⁹⁴ by high-obliquity excursions, and such ice ages may have accounted for one-quarter of the
¹⁹⁵ post-Noachian period (Forget et al., 2006; Madeleine et al., 2009; Weiss, 2019). The rates
¹⁹⁶ of deposition and ages of polar layered deposits of CO₂ also depend critically on large-scale
¹⁹⁷ obliquity oscillations (Manning et al., 2019; Emmett et al., 2020).

¹⁹⁸ 1.4 Geologic constraints on historical Mars obliquity

¹⁹⁹ Holo et al. (2018) devised a statistical-computational pipeline to constrain the post-Noachian
²⁰⁰ obliquity of Mars that exploited evidence imprinted by grazing bolide impacts upon geologic
²⁰¹ units of known age. When impactors strike Mars at a low angle of incidence, they create
²⁰² craters that are elliptic and hence oriented. In aggregate, the orientations of such elliptic
²⁰³ craters can inform us of the past obliquity of Mars; in particular, the overall distribution of
²⁰⁴ elliptic crater azimuths (orientations from due north) on Mars depends on obliquity such that,
²⁰⁵ at low obliquity, craters are more north-south oriented (low azimuth) and, at high obliquity,
²⁰⁶ they tend to be more east-west oriented (high azimuth). (The mechanics of this process are
²⁰⁷ explained further in §2.3.) Taking the azimuths of elliptic craters from the Robbins global
²⁰⁸ Mars crater database (Robbins & Hynek, 2012), Holo et al. compared the real azimuth
²⁰⁹ distribution to predicted azimuth distributions of craters generated by causing randomly
²¹⁰ seeded impactors to strike Mars, whose obliquity at the time of impact was determined by a
²¹¹ simulated obliquity history; each prediction of azimuth distribution thus corresponded to a
²¹² different simulated Mars obliquity history Kite et al. (2015). Assigning a heavier weighting to
²¹³ the histories whose predicted azimuth distributions best matched that of the actual geologic
²¹⁴ data, Holo et al. then calculated the weighted-average probability density function for the
²¹⁵ mean obliquity and fraction of time with obliquity >40°.

²¹⁶ Holo et al. (2018) concluded that, during the Hesperian, Mars's mean obliquity was
²¹⁷ likely between ~10° and ~30° (lower than the unweighted prior, i.e., the mean obliquity
²¹⁸ calculated by equally weighting all of the simulated Mars obliquity histories) and rejected

at the 95 percent confidence level that mean obliquity was $\gtrsim 33^\circ$. To produce this result, they assumed that their simulated impactors were representative of post-Noachian Mars history and were not biased in terms of inclination; that the size frequency distribution of their impactors was representative of those that have struck post-Noachian Mars; that the 1,502 craters they studied were a representative sample of all elliptic post-Noachian craters; and that geologic surface processes and crater collapse did not excessively deform crater morphologies so as to obscure crater azimuths at the time of formation. While their study produced an overall prediction of late Hesperian–onward obliquity, they could not distinguish between mirrored obliquity histories (i.e., those that start low and end high and those that start high and end low) and could not comment on Amazonian-specific Mars obliquity history. Their methodology is also difficult to apply to even earlier periods in Mars history due to the heavy degradation of craters on Noachian geologic units.

As Holo et al. (2018) pointed out, there have been few attempts to geologically constrain Mars obliquity history; relevant studies have been Earth-based and indirect or tangential. For example, Ma et al. (2017) demonstrated using an astronomical clock, developed by Sageman et al. (2014) using stratigraphic evidence from the Cretaceous Western Interior Basin, that Mars–Earth resonance transitions are chaotic, while Kent et al. (2018) used a magnetic polarity sequence from Earth to confirm the stability of the 450 ka Jupiter–Venus eccentricity cycle. Relatedly, Olsen et al. (2019) used the Geological Orrery, a systematic record of Triassic and Jurassic lake sediment deposits temporally correlated to changes in Earth’s orbital properties, to recover values for the precessions of the perihelion for Mercury, Venus, Earth, and Mars, while Mau et al. (2022) found evidence of long-term climate cycles on Earth, attributed to Earth–Mars gravitational intersections, using chronostratigraphic records. These studies offer insight into how future researchers might marshal Martian geologic evidence for the study of planetary orbital properties by emulating methods used on Earth samples, but they do not directly investigate Mars obliquity history. At present, the statistical analysis

²⁴⁵ of elliptic crater orientations and dating of ice deposits seem to be the only feasible ways to
²⁴⁶ geologically constrain Mars obliquity.

²⁴⁷ **1.5 Overview of this study**

²⁴⁸ This study attempts to constrain the mean obliquity of Mars over two time periods: ~ 0.9 Ga
²⁴⁹ ago to present and ~ 2.0 Ga ago to present. We adapt Holo et al. (2018)'s forward model
²⁵⁰ (i.e., its algorithm for generating predicted obliquity-specific azimuth distributions) to a new
²⁵¹ dataset consisting of craters in the Amazonian and Amazonian-Hesperian volcanic units. In
²⁵² §2, we detail the data collection process (§2.2), modifications to and use of Holo et al. (2018)'s
²⁵³ forward model (§2.3), statistical comparison of simulated and observed crater azimuth prob-
²⁵⁴ ability distribution functions and determination of the ages of Martian geologic units (§2.4),
²⁵⁵ and sensitivity checks (§2.5). In §3, we present our results: the simulated and observed
²⁵⁶ azimuth probability distributions (§3.1), the mismatch between simulated and observed az-
²⁵⁷ imuth probability distributions as a function of obliquity (§3.2), and the reconstructed mean
²⁵⁸ obliquity of Mars over absolute geologic time (§3.3). In §4, we first discuss the overall trends
²⁵⁹ in the results (§4.1), compare our results to those in the literature (§4.2), perform sensitivity
²⁶⁰ tests (§4.3), discuss the implications of our results for past Martian climate and hydrology
²⁶¹ (§4.4), and discuss the limitations of this study (§4.5). We conclude in §5.

262

2 METHODS

263

2.1 Overview of methods

264 This study's methods are summarized in Figure 2.1. Our procedure comprised four broad
 265 stages, of which Stages 1, 2, 3, and 4 respectively correspond with §2.2, §2.3, §2.4, and §2.5.

266 We used MATLAB version R2022a to perform data analyses and create figures (MATLAB,
 267 2022); translucent lines in figures were drawn using a custom script (Shoelson, 2012).

268

2.2 Collection of crater azimuth data

269 We focused on two units on the surface of Mars, distinguished by their composite morphology,
 270 infrared brightness, and thickness, among other factors, according to Tanaka et al. (2014): the
 271 younger late Amazonian volcanic (lAv) unit and a portion of the older Amazonian–Hesperian
 272 volcanic (AHv) unit. Note that while the lAv unit is younger than the AHv unit, the former
 273 is distinct from and not a subset of the latter; see §2.4 for how each unit was dated based
 274 on the age of the underlying rock. The lAv unit stretches from southern Elysium Planitia
 275 in the eastern hemisphere to much of Amazonis Planitia in the western hemisphere, and
 276 additionally includes Marte Vallis, peripheral areas east of Olympus Mons, and northeastern
 277 Ceranius Fossae. The AHv unit encompasses most of the Tharsis and Elysium Rises, as well
 278 as part of Amazonis Planitia. As indicated in Figure 2.2, we sampled craters in the entirety of
 279 the lAv unit and, for the AHv unit, only sampled the NW quadrant, i.e., southern Amazonis
 280 Planitia and northern Tharsis Rise.

281 This study considered craters identified in the Robbins global Mars database of 384,343
 282 Mars craters with diameters of at least 1 km Robbins & Hynek (2012). Using JMARS version
 283 5.2 (Christensen et al., 2009), analyst 1 (James Hu) traced the rims of 3,999 craters (all 1,726
 284 craters in the lAv unit, plus 2,273 craters in the AHv unit) using the “Add Points” feature in
 285 separate map layers, then exported the traces as shapefiles. We subsequently employed an

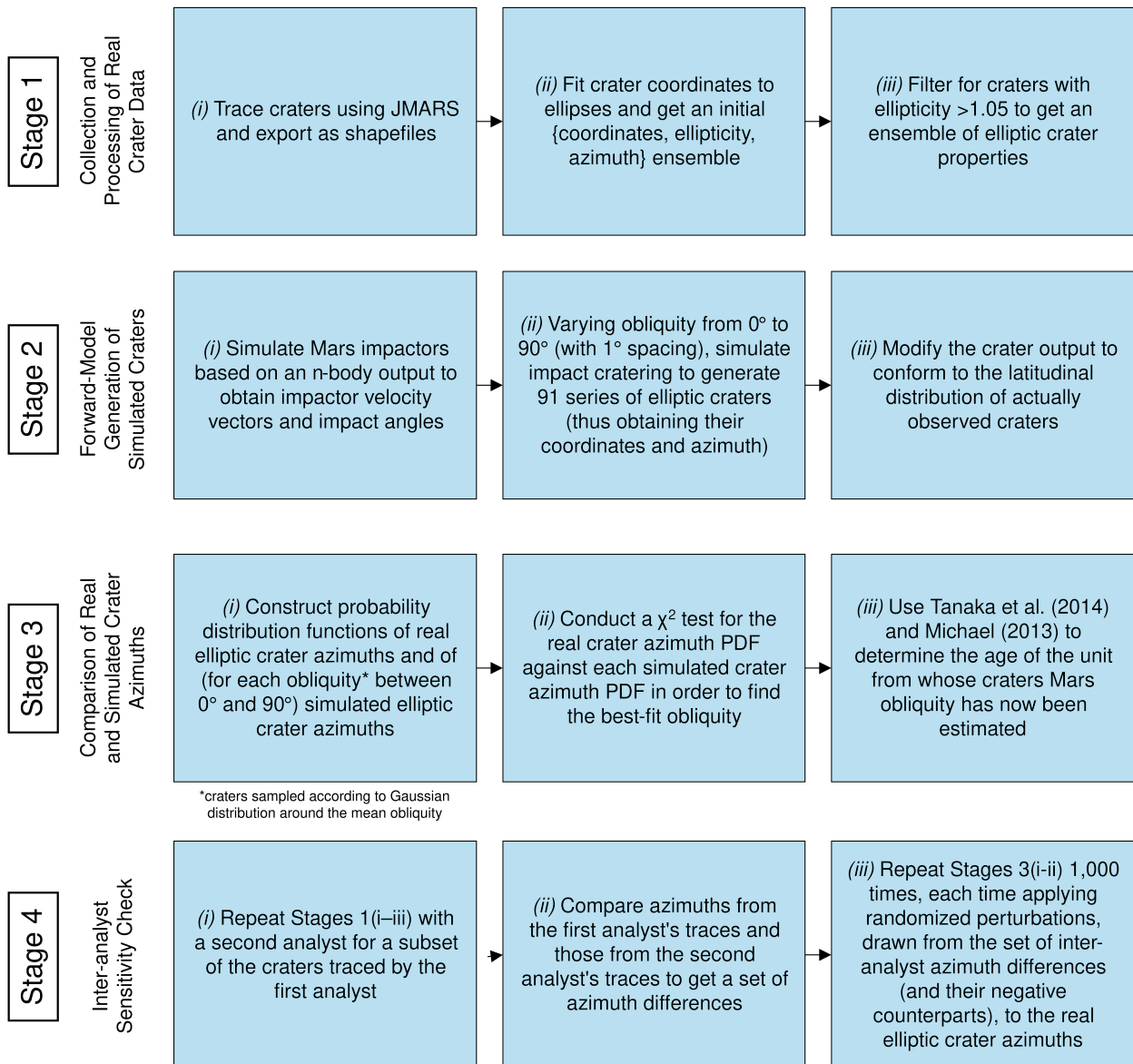
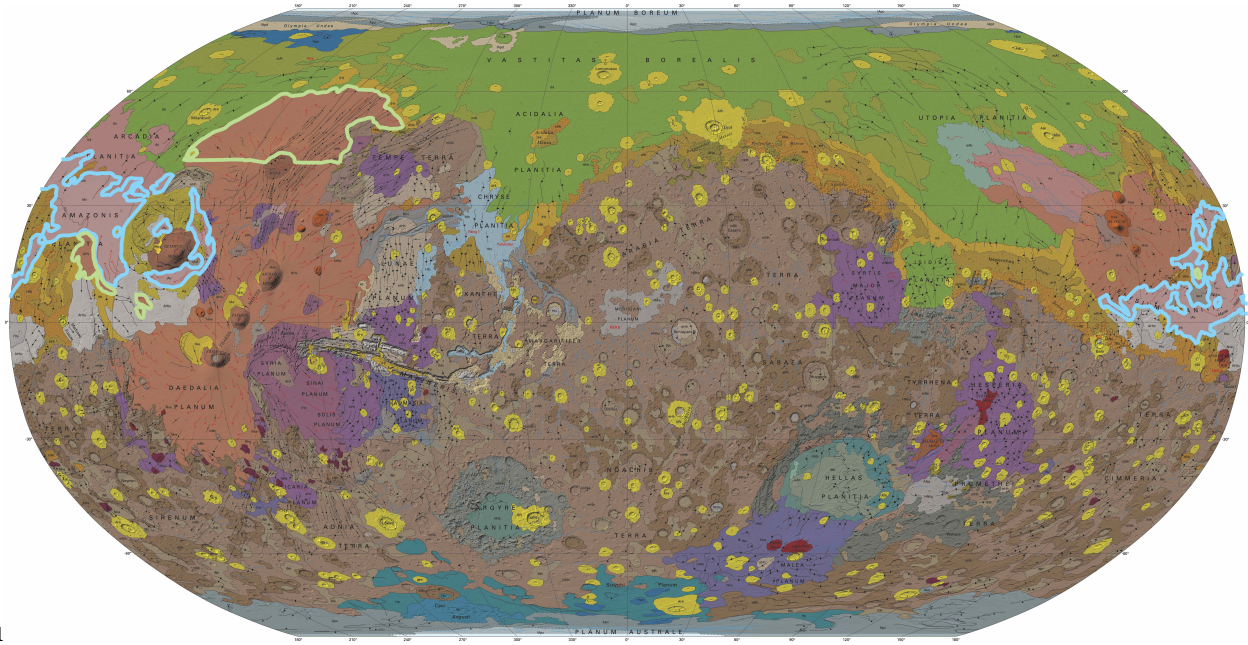


Figure 2.1: Flow chart overview of this study's methods.



1

Figure 2.2: Tanaka et al. (2014) geologic map of Mars, with sampled areas outlined: aqua outline: lAv unit; lime outline: surveyed portion of the AHv unit.

286 ellipse-fitting script to convert the shapefiles into ellipses, thus yielding data on the craters'
 287 diameters, center coordinates, ellipticities, and azimuths (Gal, 2003). For two example pairs
 288 of crater traces and ellipse fits, see Figure 2.3. Finally, we filtered the craters for an ellipticity
 289 (defined as the length of the major axis over that of the minor axis) >1.05 . As shown in
 290 Figure 2.4, most craters have ellipticity <1.05 . Including craters that are insufficiently elliptic
 291 would risk introducing large errors in crater azimuth, as even small imprecisions in tracing
 292 could cause large errors in azimuth. A threshold of 1.05 is the maximum that allows for
 293 an overall dataset size at least as large as that in Holo et al. (2018); a 1.10 threshold, for
 294 instance, would only yield 521 craters and 1.15 only 248 (see §4.3 for alternative results
 295 should our procedure have set 1.10 or 1.15 as the threshold). This made for a final dataset
 296 of 1,678 elliptic craters (761 in the lAv unit and 917 in the AHv unit).

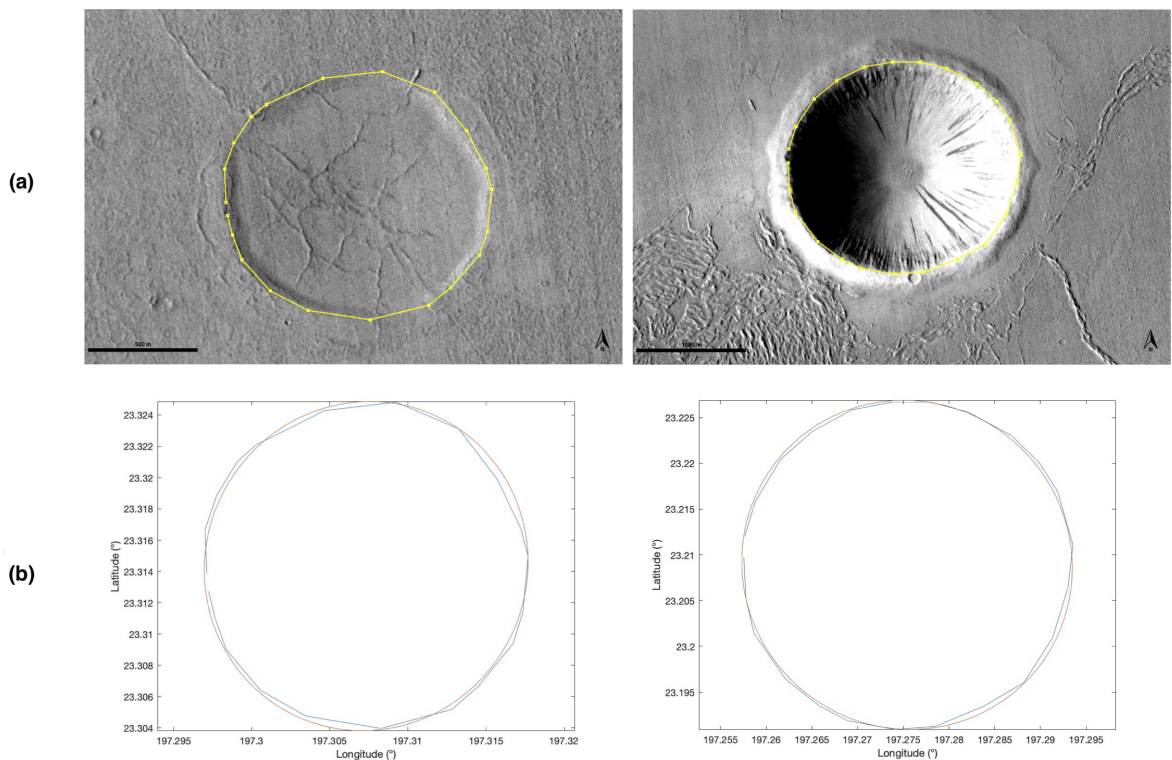


Figure 2.3: Two sampled craters in the AHv unit: (a) the crater rims are traced in JMARS 5.2; (b) the traced coordinates (blue) are fitted to smooth ellipses (orange).

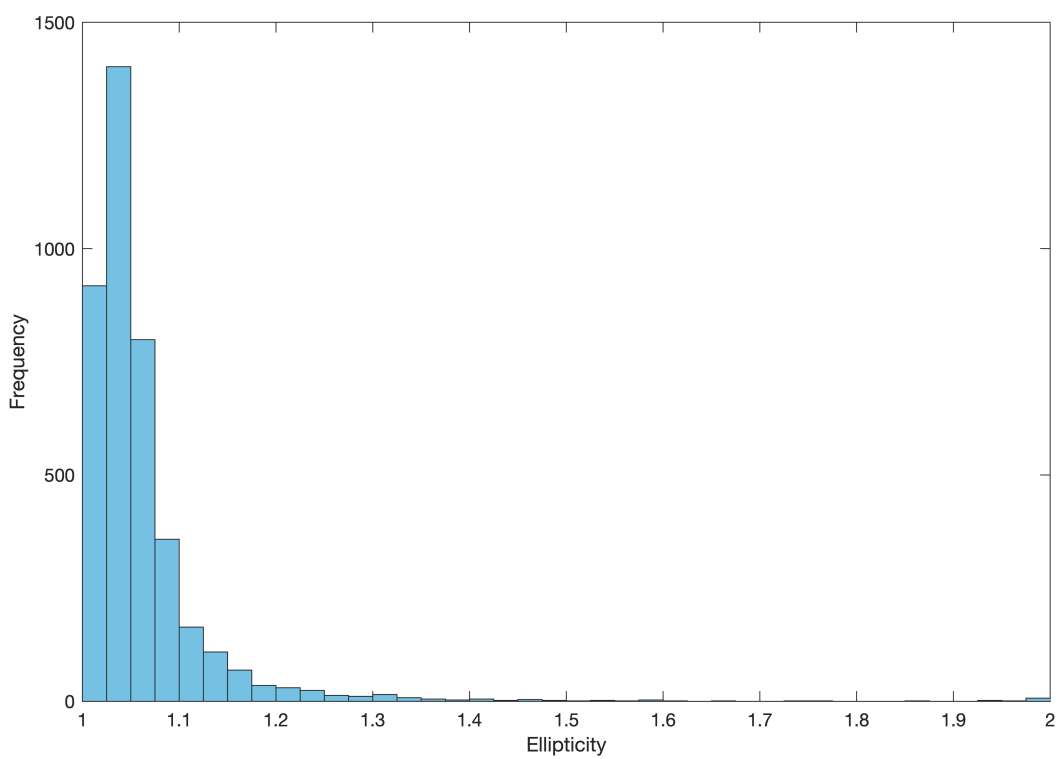


Figure 2.4: Distribution of traced crater ellipticities.

297 2.3 Adaptation of Holo et al. (2018)'s forward model

298 To generate simulated crater azimuths, we adopted and modified Holo et al. (2018)'s forward
299 cratering model. Their model consists of two parts: generating impactors and generating
300 impacts under 91 different scenarios, each corresponding to holding Mars at a constant
301 obliquity (each whole-number value in 0° – 90°) over time. Because impact rates, impact angle
302 distributions, and impact velocity distributions vary across the surface of Mars, Mars impacts
303 exhibit latitudinal variations (such that cratering is more intensive at the poles than at the
304 equator) (Le Feuvre & Wieczorek, 2008). The oscillating obliquity of Mars adds a further
305 layer of complication by shifting the positions of each latitude relative to the stream of
306 impactors; this is how the various constant-obliquity simulations exerted an effect on the
307 distribution of crater azimuths. The relationship between Mars obliquity, impactor direction
308 of travel, and azimuth of resultant crater is visually diagrammed in Figure 2.5, based on
309 Figure 1 in Holo et al. (2018).

310 To generate impactors, Holo et al. (2018) assumed a steady state in the main asteroid
311 populations, whose impacts they took to dominate the crater record on the surface of Mars
312 (Bottke et al., 2000, 2002). By running a Solar System simulation wherein modern Mars
313 crossers were test particles and the planets were massive bodies, Holo et al. retrieved 124
314 “close encounters,” defined as (the encounter speeds and encounter inclinations of) objects
315 that passed within one Hill radius of Mars during the 10 Ma integration. From their 124
316 close encounters, we simulated 10^6 impacts, then selected those resulting in elliptic crater
317 formation (\sim 80,000). These were then pared down to craters with diameters of at least
318 4 km (\sim 20,000), whose latitude and azimuth were determined for 91 hypothetical constant-
319 obliquity scenarios (each whole-number value in 0° – 90°). The forward model therefore yielded
320 an initial $91 \times \sim 20,000$ ensemble of elliptic crater azimuths, organized by constant-obliquity
321 scenario. The impacting model is visually diagrammed in Figure 2.6, based on Figure 6 in
322 (Holo et al., 2018).

Unlike Holo et al. (2018), we subsequently tuned the initial output of the forward model such that the latitudinal distribution of the simulated craters better resembled that of collected crater data (§2.2). While the 1,502 craters studied by Holo et al. (2018) spanned most of the latitudinal extent of Mars, this study’s measured (real) craters were located within specifically defined latitudinal boundaries. In the interest of having our simulated craters’ latitudinal distribution match that of our real craters, we devised a resampling procedure to normalize the simulated latitudinal distribution of craters to the empirical latitudinal distribution. The procedure entailed, first, sorting simulated craters into 5° -wide latitude bins and comparing the frequency of simulated craters within each latitude bin to the frequency of real craters within each latitude bin. (This procedure was applied for both the lAv and AHv units, which have different latitudinal distributions of craters, thereby resulting in two distinct sets of simulated craters.) Second, a scaling parameter was determined for each latitude bin as the empirical (i.e., desired) crater frequency divided by the simulated (i.e., pre-normalization) crater frequency. This scaling parameter was then divided by the maximum scaling parameter over all the latitude bins to yield a scaling factor ≤ 1 . Third, craters were resampled for each latitude bin; a random sample (without replacement) of the craters in each latitude bin was retained, and the rest discarded, where the proportion retained was the scale factor. Recall that there are two geologic units and 91 constant-obliquity scenarios; this procedure was therefore repeated for each geologic unit and each scenario separately. Finally, we scaled up the number of craters to 10^6 , by repeatedly randomly sampling (with replacement) the post-normalization set of craters, for each constant-obliquity scenario and each geologic unit, such that each final simulated crater ensemble had dimensions 91×10^6 .

2.4 Determination of best-fit obliquity and geologic unit age

Similar to Figure 7 in Holo et al. (2018), we constructed crude probability density functions (i.e., histograms with bin width 10°) of the simulated crater azimuth distributions, one each

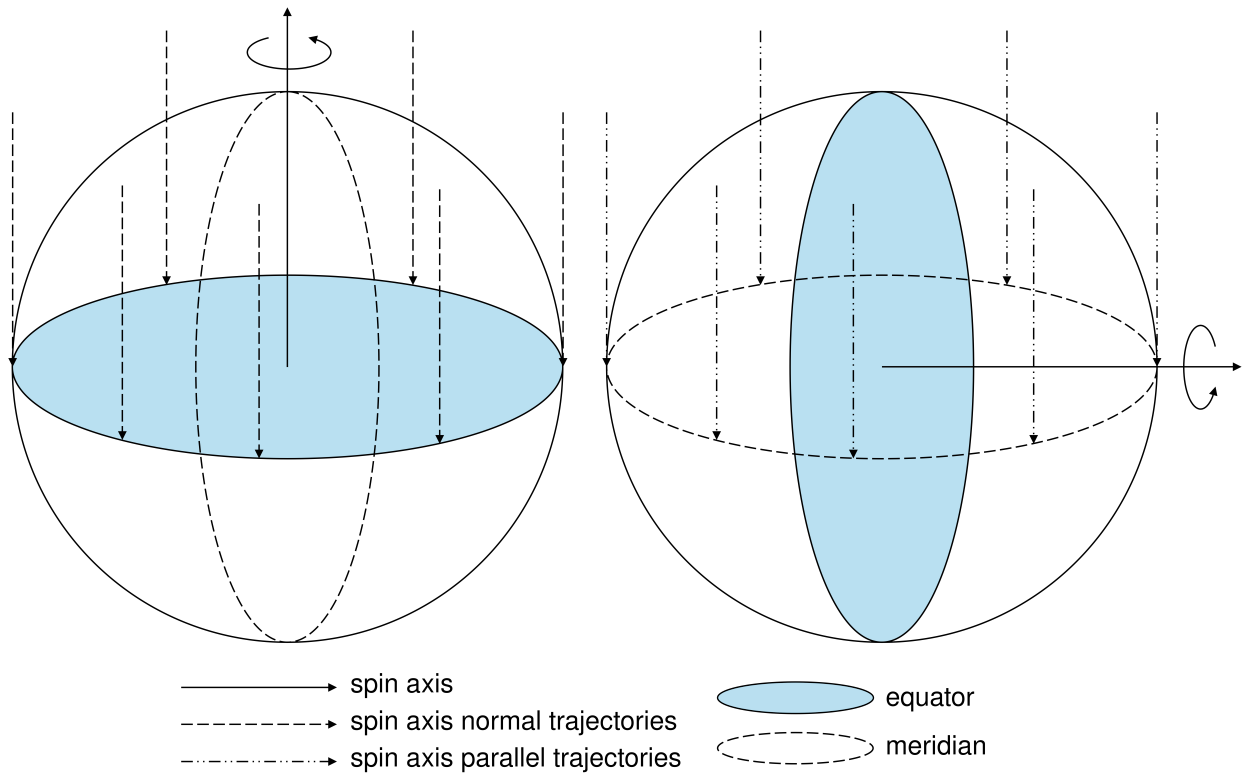


Figure 2.5: Physical basis for variation in elliptic crater azimuth distribution by planetary obliquity scenario (north-south azimuths at low obliquity, left, and east-west azimuths at high obliquity, right). Meridian refers to any circle in the plane perpendicular to the equatorial plane. Based on Figure 1 in Holo et al. (2018).

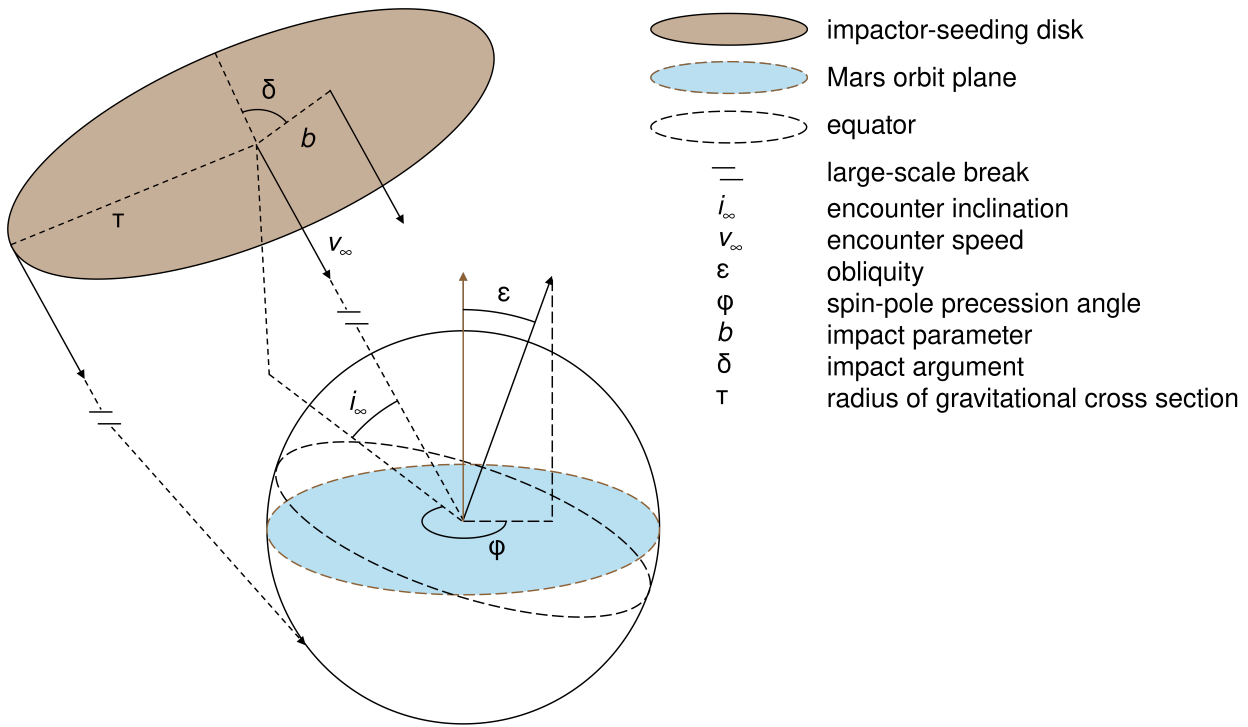


Figure 2.6: Schematic representation of the impact simulation model, wherein impactors are seeded in the disk and create craters on a location on Mars that varies with Mars obliquity. Because impactors are assumed to follow an orbit about the center of Mars that conserves angular momentum (Le Feuvre & Wieczorek, 2008), all impactors within a disk with radius τ , for a given $\{i_\infty, v_\infty\}$, impact the surface. Note that the depicted impactor-seeding disk is only one of 124 such random disks, and impactors do not necessarily come at Mars from a specific angle to the orbital plane. Based on Figure 6 in Holo et al. (2018).

348 for the lAv unit and the AHv unit. These represented the crater azimuth distributions we
349 would expect to observe in our data given various hypothetical constant Mars obliquities.
350 This alone would be insufficient to model Mars obliquity, however, because Mars obliquity
351 has continuously oscillated.

352 To model the periodic (non-secular) oscillations of Mars obliquity, we therefore calculated
353 the standard deviation of the past 2.5 Ma of Mars obliquity history, which we found to be
354 5.03° (Laskar et al., 2010). Applying this result, we resampled each constant-obliquity crater
355 azimuth ensemble to fit a Gaussian distribution with its mean as the original obliquity
356 and its standard deviation as 5.03° . Recall that the ensemble has dimensions 91×10^6 ; this
357 resampling procedure was repeated for each 10^6 set of craters such that the post-resampling
358 set would consist of a mixture of craters from neighboring obliquities. For example, the
359 resampled ensemble for 75° obliquity would consist of 10^6 craters drawn, according to a
360 Gaussian distribution centered around 75° , from a mixture of obliquity scenarios, such that
361 ~ 68 percent of the craters would come from obliquity scenarios between $\sim 70^\circ$ and $\sim 80^\circ$ and
362 ~ 95 percent of them would come from those between $\sim 65^\circ$ and $\sim 85^\circ$. (Resampling also had
363 the effect of significantly smoothing the subsequent χ^2 tests that we performed.)

364 We applied the same procedure to construct histograms of the actual crater azimuth dis-
365 tributions, also finding the standard deviation, for each geologic unit. We then implemented
366 91 χ^2 tests (one per obliquity scenario) for each geologic unit, comparing the simulated
367 crater azimuth distributions to the real crater azimuth distributions. We took the obliquities
368 for which the reduced χ^2 statistic was at a minimum to be the best-fit mean obliquities,
369 for each geologic unit. Using an curve intersection–finding script (Schwarz, 2017), we then
370 found one-standard deviation confidence intervals graphically by determining the obliquities
371 corresponding to a reduced χ^2 statistic $\sqrt{2(8)}/8 = 0.5$ higher than the minimum (see §3.2).
372 Note that the variance of χ^2 is defined as 2ν where ν is the number of degrees of freedom
373 (in this case, there were nine bins and one independent parameter, so $\nu = 9 - 1 = 8$); the

³⁷⁴ standard deviation of reduced χ^2 is therefore 0.5.

³⁷⁵ The geologic units are described by Tanaka et al. (2014) as dating to the late Amazonian
³⁷⁶ and Amazonian–Hesperian periods, respectively. To assign an absolute numeric age to each
³⁷⁷ unit, however, we employed the isochron fitting criteria in Table 2 of Michael (2013), based
³⁷⁸ on Martian epoch boundaries specified by Hartmann (2005). This entailed retrieving the
³⁷⁹ density of craters with diameters larger than the relevant reference crater diameter (1 km)
³⁸⁰ from Tanaka et al. (2014), dividing that value by the relevant upper crater density boundary,
³⁸¹ and multiplying the fraction by the start of epoch specified by Hartmann (2005).

³⁸² 2.5 Sensitivity checks

³⁸³ As a primary sensitivity check, we reran the analyses to account for inter-analyst error in
³⁸⁴ tracer azimuth tracing. The error in tracing was quantified by 23 repeat traces of craters
³⁸⁵ by analyst 2 (Edwin Kite) in the AHv, using JMARS version 5.2, of which five were found
³⁸⁶ to be elliptic based on the 1.05 threshold. In addition, we searched the 1,502 elliptic craters
³⁸⁷ from Appendix C in Holo et al. (2018), sourced from the Robbins & Hynek (2012) database,
³⁸⁸ finding four which analyst 1 had traced in the procedure outlined in §2.2. We thus computed
³⁸⁹ the nine differences between the azimuth values of analyst 1’s original traces with analyst
³⁹⁰ 2’s and with those used by Holo et al. (2018). We then applied at random an inter-analyst
³⁹¹ perturbation (one of the nine differences, or their negative counterpart, such that there
³⁹² were 18 options for perturbation) to each crater azimuth (see §4.3). In practice, this meant
³⁹³ iterating through analyst 1-traced crater azimuths and randomly adding or subtracting one
³⁹⁴ of the nine inter-analyst differences to create a new set of crater azimuths. The perturbed
³⁹⁵ dataset was then passed through the same procedure outlined in §2.4 for comparison with
³⁹⁶ simulations. As an additional sensitivity check, we also reran the analyses, filtering traced
³⁹⁷ craters using various threshold ellipticities (the default 1.05, as well as the higher thresholds
³⁹⁸ of 1.10 and 1.15, in addition to the no-threshold case, 1.00, included for interest).

3 RESULTS

400 3.1 Simulated and observed crater azimuth distributions

401 Figure 3.1 shows the simulated and actual crater azimuth distributions, represented by line
 402 plot histograms, for the lAv unit and AHv units. For clarity, only select obliquity scenarios
 403 are shown. Both the original crater data and the inter-analyst-perturbed data are shown.

404 3.2 Simulated–observed crater azimuth distribution comparisons

405 Figure 3.2 shows the extent of mismatch (the reduced χ^2 statistic) of each Gaussian-smoothed
 406 obliquity scenario, for each geologic unit, where a lower mismatch ~ 1 indicates a better
 407 simulation–data fit. Both the results from the original crater data and those from the inter-
 408 analyst-perturbed data are shown. The results of the χ^2 tests are summarized in Table 3.1.

409 3.3 Mean obliquity of Mars over geologic time

410 Table 3.2 summarizes the absolute unit ages of each geologic unit. Figure 3.3 summarizes
 411 the mean obliquity over time corresponding to each geologic unit, based on simulation–data
 412 comparisons from §3.2, also plotting the deterministic reverse integrations provided by Laskar
 413 et al. (2010).

Table 3.1: Summary of results of χ^2 tests between simulated crater azimuth distributions and the observed crater azimuth distribution.

Geologic unit	Description	Lower bound (°)	Best fit (°)	Upper bound (°)
lAv	Original trace	56.2	66	74.6
	Inter-analyst-perturbed	54.7	63	72.0
AHv	Original trace	0.0	8	14.4
	Inter-analyst-perturbed	6.3	14	20.5

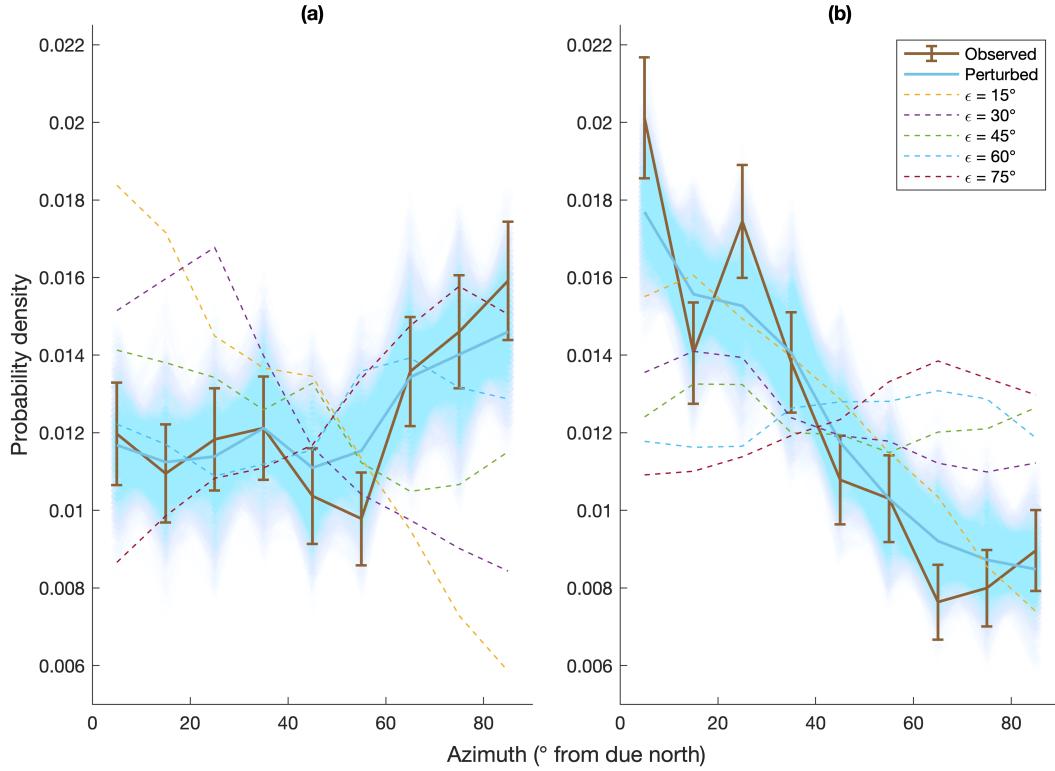


Figure 3.1: Distribution of simulated and observed crater azimuths for the (a) lAv and (b) AHv units. Dotted lines: simulated, Gaussian-resampled, latitude distribution–normalized obliquity scenarios for different mean obliquities, ϵ ; translucent turquoise lines: 1,000 random instances of inter-analyst-perturbed observed crater azimuths; solid blue line: median of the 1,000 perturbed azimuths.

Table 3.2: Absolute ages of sampled geologic units.

Geologic unit	Density of craters with diameter >1 km, $N(1)$ (per Mkm^2)	Absolute age (Ga)
lAv	551.8 ± 12.7	0.947 ± 0.022
AHv	$1,303.3 \pm 9.9$	2.011 ± 0.015

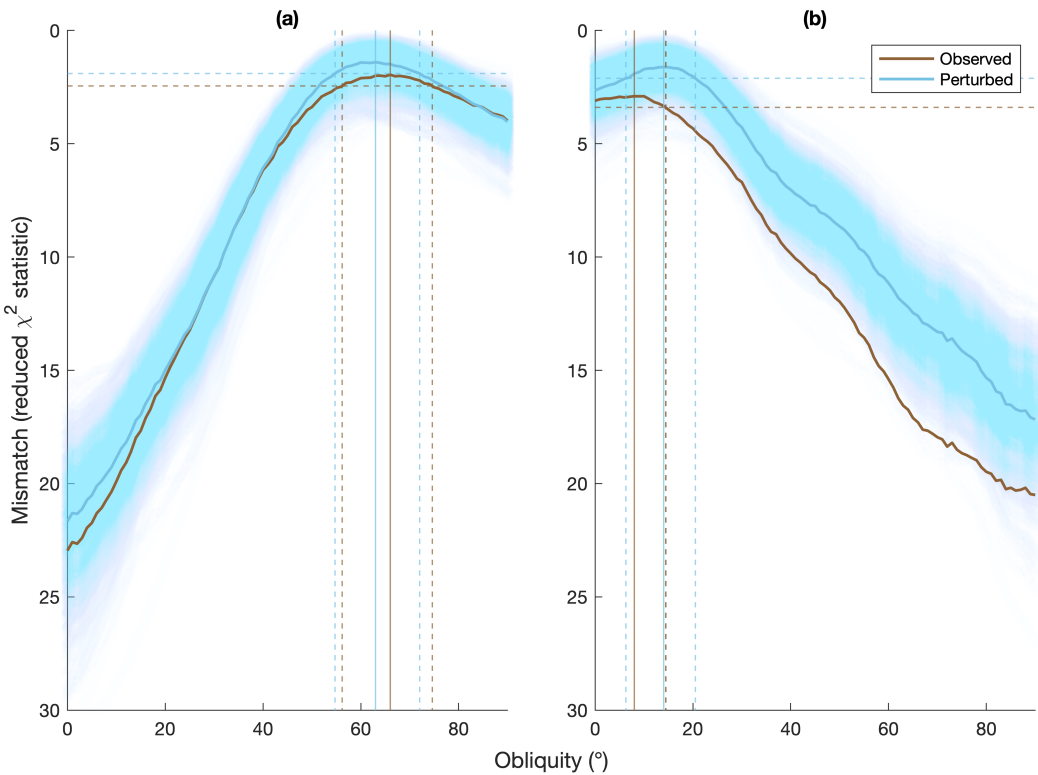


Figure 3.2: Mismatch (reduced χ^2 statistic) between the crater azimuth distribution of each Gaussian-smoothed obliquity scenario and the observed crater azimuth distribution for the (a) 1Av and (b) AHv units. Translucent turquoise lines: 1,000 random instances of inter-analyst-perturbed observed crater azimuths; solid blue line: median of the 1,000 perturbed azimuths; central, solid vertical lines: best-fit obliquity, corresponding to the minimum reduced χ^2 statistic; the dotted vertical lines: confidence interval.

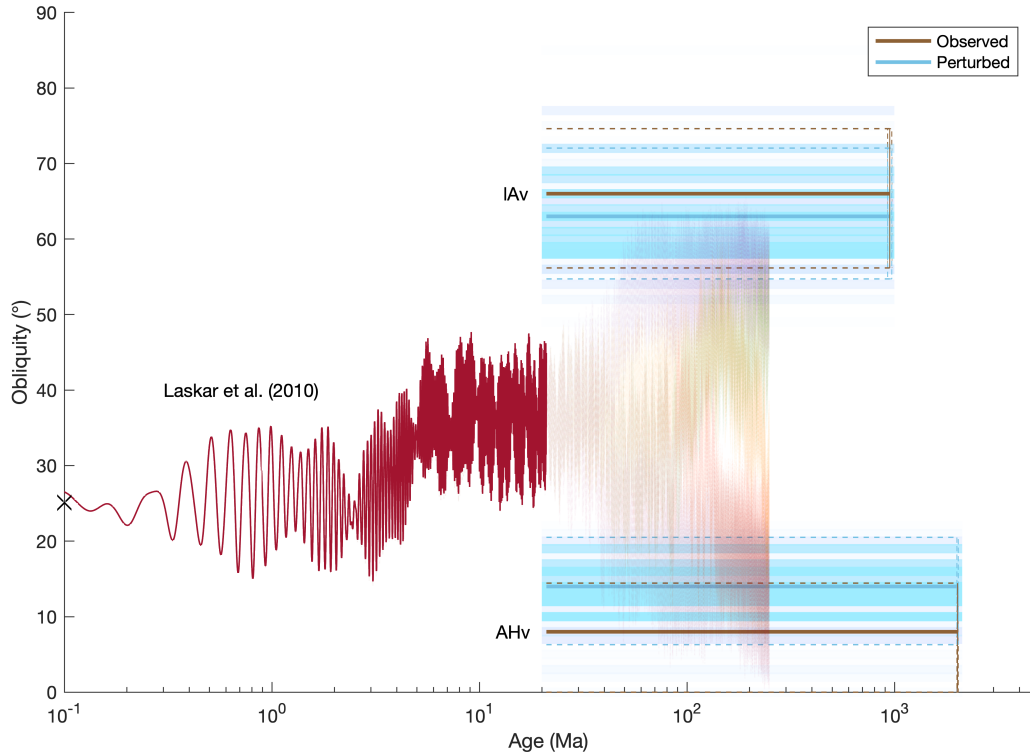


Figure 3.3: Mean obliquity of Mars over time (logarithmic scale). Translucent turquoise: estimates based on 1,000 random instances of inter-analyst-perturbed observed crater azimuths; blue: best-fit mean obliquity for the median of the 1,000 perturbed azimuths (solid line: best fit; dotted lines: upper and lower confidence bounds with respect to standard deviation); brown: best-fit mean obliquity estimates for the original crater traces (solid line: best fit; dotted lines: upper and lower bounds with respect to standard deviation); black cross: present-day obliquity (25.1°); burgundy: Laskar et al. (2010)'s deterministic reverse integration; other translucent lines: five chaotically diffusive reverse integrations to 249 Ma ago, demonstrating that large swings in Mars obliquity, due to secular spin-orbit resonances, make it impossible to precisely reverse-integrate its history beyond ~ 100 Ma.

414

4 DISCUSSION

415

4.1 Synthesis of results

416 Simulations of Mars crater azimuths exhibit a pattern whereby the crater population is more
 417 north-south oriented at lower obliquities and more east-west oriented at higher obliquities
 418 (Figures 2.5, 3.1). This pattern (of sensitivity of azimuth distribution to obliquity) holds
 419 much more strongly for the lAv unit than for the AHv unit. In other words, for the lAv unit,
 420 histograms show that more extreme obliquities are associated with more lopsided (heavily
 421 north-south or east-west oriented) azimuth distributions; by contrast, for the AHv unit,
 422 histograms for obliquities 30°, 45°, 60°, and 75° all show roughly flat azimuth distributions.
 423 The simulations for the two geologic units only differ because crater samples were sourced
 424 from different latitudes: craters in the lAv unit spans latitudes ∼0–45° (north and south
 425 were folded), while traced craters in the AHv unit comprise separate low-latitude (∼0°–25°)
 426 and high-latitude (∼40–65°) subsets (Figure 4.1); it thus appears that higher-latitude crater
 427 azimuths are less sensitive to obliquity.

428 As shown in Figure 3.3, Mars’s recent (past ∼100 Ma) obliquity trajectory lies between an
 429 early historical (past ∼2.0 Ga) low period, followed by a later historical (past ∼0.9 Ga) high
 430 period. In particular, Figure 3.2 indicates statistically that Mars’s mean obliquity recorded on
 431 the lAv unit (i.e., since ∼0.9 Ga ago) has likely been very high, at ∼66° (56.2°–74.6° standard
 432 deviation interval), and that recorded on the AHv unit (i.e., since ∼2.0 Ga ago) very low, at
 433 ∼8° (0.0°–14.4° standard deviation interval). For the AHv specifically (Figure 3.2b), there is
 434 also an especially notable offset between the mismatches of the inter-analyst-perturbed and
 435 those of non-perturbed crater azimuth data, possibly due to the more extreme azimuths, and
 436 consequently more extreme mean obliquity, determined from the non-perturbed crater data
 437 (see §4.3). For each geologic unit, the smallest χ^2 value, implying the least mismatch, is not
 438 sharply defined. Indeed, although standard deviation confidence intervals are defined more

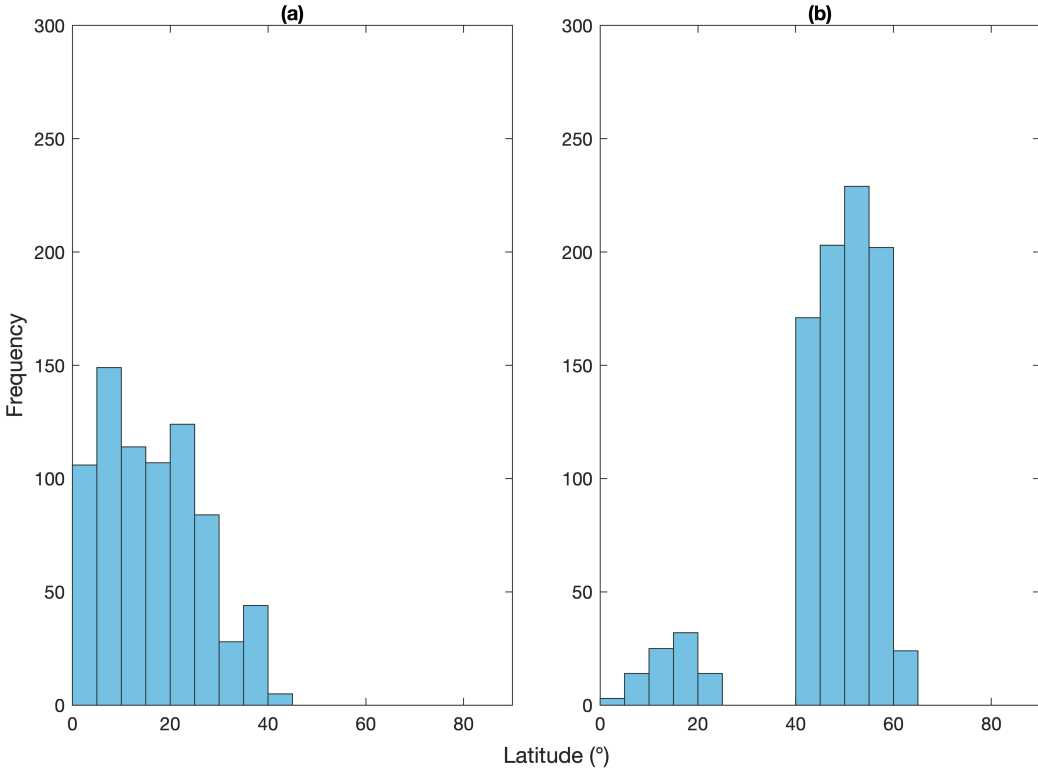


Figure 4.1: Frequency histogram showing the number of elliptic craters traced per 5° latitude bin for the (a) lAv and (b) AHv units.

precisely, very low χ^2 values (<5) are observed through the high obliquity range of $\sim 40^{\circ}$ and up for the lAv unit, and likewise through the low obliquity range of $\sim 25^{\circ}$ and under for the AHv unit. This study is consequently unable to rule out large swaths of possible past mean obliquities, although the result that the older unit is associated with lower obliquity than the younger unit is clear.

4.2 Comparison with previous studies

Holo et al. (2018) estimated that the mean obliquity over the past ~ 3.5 Ga was likely between $\sim 10^{\circ}$ and $\sim 30^{\circ}$. The standard-error interval of our best-fit mean obliquity approximation for the older AHv unit, 0.0° to 14.4° , aged ~ 2.0 Ga, is consistent with, albeit firmly at the lower

end, of the previous estimate. It is possible that a higher-obliquity excursion from \sim 3.5 Ga ago to \sim 2.0 Ga ago could have pulled the mean obliquity to a higher value for the entire post–late Hesperian period, which could be investigated using older geologic units. However, Holo et al. also estimated that the fraction of time spent at obliquities $>40^\circ$ was less than one-fifth of the time since \sim 3.5 Ga ago. This is most likely inconsistent with our 56.2° to 74.6° mean obliquity estimate for Mars since \sim 0.9 Ga ago, which represents well over one-fifth of the time elapsed since \sim 3.5 Ga ago.

While our impacting forward model was based on that of Holo et al. (2018), we employ different methods for comparing forward-model simulated crater data and real crater data. Holo et al. assigned weightings to different obliquity histories based on how many times each history provides the best fit (using the two-sample Kolmogorov–Smirnov test) to a bootstrapped sample of the real crater data, then take the weighted averages of those obliquity histories to find the mean obliquity since \sim 3.5 Ga ago. By contrast, this study instead makes direct comparisons between the simulated crater azimuth distributions, for each whole-number value of obliquity in 0° – 90° , and the real crater azimuth distributions. Further research should therefore cross-examine these studies’ methodologies by applying the method of Holo et al. (2018) to our data, and vice versa, to investigate the extent to which methodological differences explain the likely inconsistencies in outcome.

Laskar et al. (2010) additionally provided five solutions to 249 Ma ago in order to demonstrate the chaotic diffusion of Mars obliquity at >100 Ma timescales. Of these, two solutions exhibited relatively low mean obliquities ($\sim 27^\circ$ and $\sim 20^\circ$), while three solutions exhibited relatively high mean obliquities ($\sim 39^\circ$, $\sim 51^\circ$, and $\sim 41^\circ$); however, none had a periodic mean obliquity $>60^\circ$ (Figure 3.2a). While these chaotic backward integrations do not give any indication of the validity of our results, they demonstrate that high-obliquity excursions are a feasible outcome of chaotic obliquity variation, thus indicating that a 56.2° to 74.6° mean obliquity since \sim 0.9 Ga cannot be *a priori* ruled out.

474

4.3 Sensitivity tests

475 First, we performed inter-analyst sensitivity tests showing that our results were robust to
 476 random perturbation, even though the inter-analyst comparison of elliptic crater azimuths
 477 revealed significant discrepancies (Figures 3.1, 3.2, 3.3; Table 3.1). As Table 4.1 shows, three
 478 of the nine elliptic craters retraced by analyst 2 or also available in Appendix C of Holo et al.
 479 (2018) yielded a greater-than-15° azimuth difference when compared with analyst 1’s original
 480 traces. However, it is unlikely that these resulted from systematic biases, because non-analyst
 481 1 azimuths are not uniformly larger or smaller than analyst 1 azimuths. Differences in traced
 482 elliptic crater azimuths could have arisen from eroded or unclear crater rims, as well as from
 483 quirks in Gal (2003)’s ellipse-fitting script.

484 The inter-analyst-perturbed results were generally more moderate (i.e., indicating obliqui-
 485 ties further from the extremes of 0° and 90°) than the results based on the original traces.
 486 This was due to the symmetric nature of azimuths; for example, given an absolute inter-
 487 analyst difference of 20°, perturbing an azimuth of 85° by +20° would result in a new azimuth
 488 of 75°, while perturbing it by -20° would result in a new azimuth of 65°; either way, the
 489 new azimuth would be further from the extremes of 0° to 90°. In addition, the inter-analyst-
 490 perturbed results generally exhibit better fits with the simulated azimuth distributions, with
 491 smaller χ^2 values uniformly for all obliquities and both geologic units (Figure 3.2).

492 Further consideration of the implications of §4.1—that over the past \sim 2.0 Ga the mean
 493 obliquity was just 8°, but that over that past \sim 0.9 Ga it was 66°—in fact necessitates the
 494 inclusion of the inter-analyst-perturbed results in the overall results for the study’s conclu-
 495 sions to be feasible: since obliquities range from 0° to 90°, the \sim 1.06 Ga period extending
 496 from \sim 2.0 Ga ago to \sim 0.9 Ga ago would have to have had a negative mean obliquity, which
 497 is unphysical. This inconsistency possibly reflects methodological problems, including the
 498 imprecise tracing and unrepresentative selection of craters (such that the observed azimuths
 499 were too extreme); the incorrect dating of geologic units (for instance, dating the lAv unit

Table 4.1: Inter-analyst variability in traced elliptic crater azimuths.

Crater No.	1	2	3	4	5	6	7	8	9
Analyst 1 (°)	54.7	56.9	29.0	60.1	22.1	23.6	63.2	28.0	21.2
Analyst 2 (°)	22.7	61.2	22.5	50.7	40.4				
Holo et al. (2018) (°)						49	62	31	19
Absolute difference (°)	32.0	4.4	6.5	9.4	18.3	25.4	1.2	3.0	2.2

500 to be substantially younger than ~ 0.9 Ga, e.g., ~ 0.20 Ga, would result in a positive mean
 501 obliquity during the intervening ~ 1.81 Ga period from ~ 2.0 Ga ago to ~ 0.20 Ga ago); and
 502 possible issues with the forward model (see §4.5).

503 Second, as discussed in §2.2, we tested the effect of varying the ellipticity threshold (1.05
 504 in our main procedure) on our results. Filtering for craters with ellipticity >1.10 (yielding 521
 505 craters) and >1.15 (yielding 248), we found decreasingly similar crater azimuth distributions
 506 for each geologic unit (Figure 4.2). Note that, because only two of the nine craters whose
 507 inter-analyst variability was quantified had ellipticity >1.10 , we were not able to perform
 508 inter-analyst sensitivity checks on the 1.10- and 1.15-threshold results. With a 1.10 ellipticity
 509 threshold, we found mean obliquities associated with the AHv, at 1° (0.0° to 17.6 standard
 510 deviation interval), and with the lAv, at 53° (42.0° to 75.3° standard deviation interval), to be
 511 lower than our 1.05-threshold results; while with a 1.15 threshold, we found mean obliquities
 512 of 0° (0.0° to 30.0° standard deviation interval) and 45° (25.9° to 65.0° standard deviation
 513 interval), respectively (Table 4.2). These tests indicate a negative relationship of ellipticity
 514 threshold with mean obliquity associated with the lAv and no clear relationship with mean
 515 obliquity associated with the AHv; however, it is likely that sample sizes become too small
 516 to draw conclusions from thresholds beyond 1.05, as shown by the increasing flatness of
 517 the reduced χ^2 statistic distributions (Figure 4.3). For interest, results for the no-threshold
 518 case are also given.

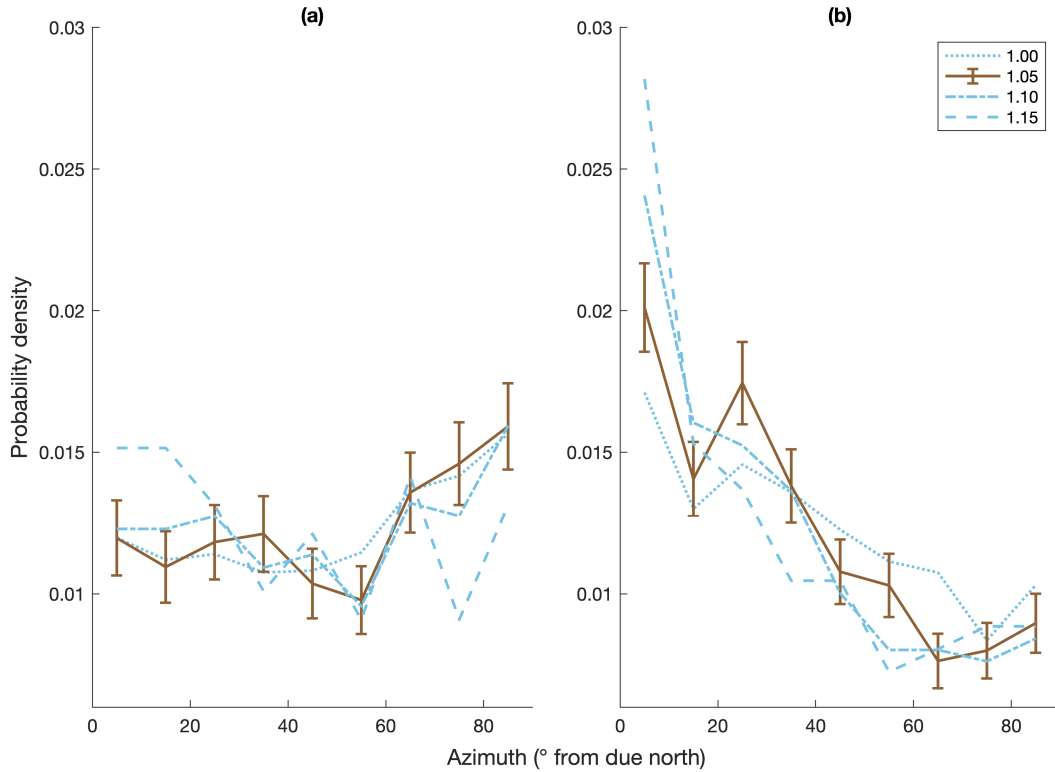


Figure 4.2: Distribution of observed crater azimuths for various ellipticity thresholds, for the (a) lAv and (b) AHv units.

Table 4.2: Summary of results of χ^2 tests between simulated crater azimuth distributions and the observed crater azimuth distribution for various threshold ellipticities.

Threshold ellipticity	Geologic unit	Crater count	Lower bound (°)	Best fit (°)	Upper bound (°)
1.00	lAv	1,726	59.2	65	69.7
	AHv	2,273	19.1	22	26.4
1.05	lAv	761	56.2	66	74.6
	AHv	917	0.0	8	14.4
1.10	lAv	244	42.0	53	75.3
	AHv	277	0.0	4	11.9
1.15	lAv	110	25.9	45	65.0
	AHv	138	0.0	0	30.0

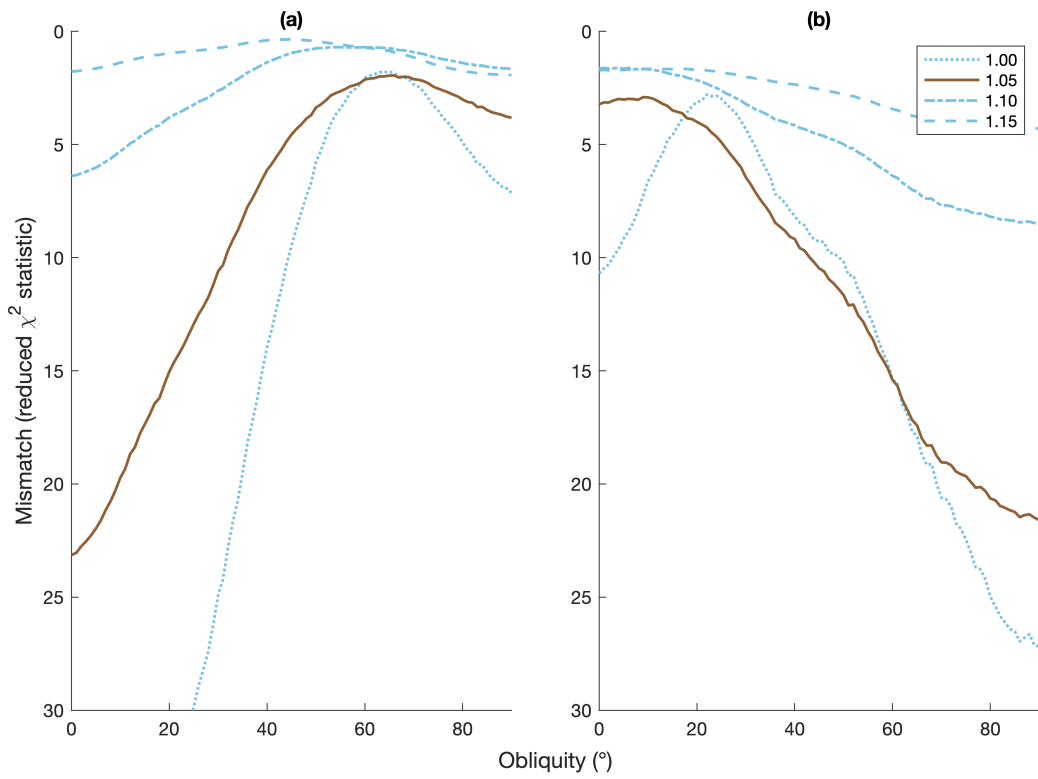


Figure 4.3: Simulated–observed crater azimuth distribution mismatch (reduced χ^2 statistic) for various ellipticity thresholds, for the (a) lAv and (b) AHv units.

519

4.4 Implications of results

520 As reviewed in §1.3, the implications for surface volatiles on Mars of high and low obliquity
 521 excursions are well understood (reviewed in Jakosky, 2021) and are caused by changes in
 522 insolation patterns by latitude: the higher latitudes receive more, and the lower latitudes
 523 receive less, insolation at higher obliquity, and vice versa. Our results indicate that Mars
 524 has experienced extensive high and low obliquity periods in its distant geologic past, such
 525 that a number of scenarios are possible. For instance, during its earlier low-obliquity period
 526 associated with the AHv unit, when its poles would have been better shielded from the Sun,
 527 Mars may have been more likely to harbor extensive glacial ice sheets at its poles, thus
 528 thinning out the atmosphere by precipitating gaseous CO₂ and causing atmospheric collapse
 529 at the poles, while also experiencing greater desiccation of deep aquifers (Lindner & Jakosky,
 530 1985; Kreslavsky & Head, 2005; Phillips et al., 2011; Soto et al., 2015; Grimm et al., 2017);
 531 while, during its later high-obliquity period associated with the lAv unit, Mars may have
 532 seen greater sublimation of water ice, the migration of water ice to its lower latitudes, and
 533 a higher water vapor pressure, in addition to more frequent polar dust storms (Haberle &
 534 Jakosky, 1990; Jakosky et al., 1995; Zent, 2013; Forget et al., 2017).

535 Fassett et al. (2014), studying craters superposed on glacial deposits, triangulated the
 536 timing of the extensive deposition of ice in the mid-latitudes to the middle to late Amazonian.
 537 Because this latitudinal pattern of ice deposition is associated with relatively high obliquities,
 538 their result suggests that the mean middle to late Amazonian obliquity was relatively high.
 539 Our result is consistent with Fassett et al. (2014) insofar as it indicates a high ($\sim 68^\circ$) mean
 540 obliquity since ~ 0.9 Ga ago. However, our result is contradicted by more recent research on
 541 upper bounds on post-Noachian high-obliquity periods (Weiss, 2019). By examining the size-
 542 frequency distribution of craters formed in surface ice, Weiss (2019) found that mid- and low-
 543 latitude ice ages account for up to ~ 25 percent of the post-Noachian geologic history of Mars.
 544 While Weiss (2019)'s results do not constitute a direct past-obliquity reconstruction, they do

545 suggest upper bounds on high-obliquity excursions, which are associated with equatorial and
546 mid-latitude ice ages, in particular, that Mars obliquity has been $\geq 45^\circ$ for at most 250 Ma
547 (corresponding to equatorial ice ages), and in the range of $\sim 30\text{--}40^\circ$ for at most 680 Ma
548 (corresponding to mid-latitude ice ages), since 3.6 Ga ago. This is inconsistent with our
549 result from the lAv unit that the mean obliquity since ~ 0.9 Ga ago has been $\sim 68^\circ$.

550 **4.5 Limitations of this study**

551 A major limitation of this study is the small number of elliptic craters (1,678) used to build
552 azimuth distribution functions, as well as the incomplete sampling of the AHv unit. The
553 precision of tracing (inter-analyst error) further imposes a limit on the accuracy of the result,
554 although the constrained obliquities appear to be robust to inter-analyst error. Additionally,
555 during the tracing process, we did not seek to account for poke-throughs of older craters
556 through geologically younger volcanic deposits. The potential presence of older craters on
557 younger terrain may have caused unquantified errors in the crater azimuth distributions,
558 thus implying that the obliquities fitted would be correct but that the ages to which the
559 obliquities apply would be too young. One factor that makes this likely is that the unit ages
560 quantified through §2.4, using Michael (2013)'s technique, do not actually correspond with
561 the names of the units given by Tanaka et al. (2014); for instance, "late Amazonian" generally
562 refers to the past ~ 0.3 Ga, not ~ 0.9 Ga, of Mars history.

563 As this study makes extensive use of Holo et al. (2018)'s pipeline, many of the limitations
564 pertaining to their study are applicable here as well. For instance, while inter-analyst error
565 is quantified, this does not preclude the possibility that lighting angle, among other factors,
566 could have caused systematic biases for both analysts that were not quantified in this study.
567 The light source originates from the west, casting a strong shadow near the western rim
568 of craters and in some cases obfuscating the eastern rim, thus making crater rims more
569 difficult to trace precisely in the east. If the net result is that analysts therefore tend to

shift the eastern rim eastward in their traces, this would bias crater azimuths toward a more heavily east-west (i.e., higher azimuth) distribution (thus implying a bias toward higher obliquities), and vice versa. A cursory analysis of all 1,678 elliptic craters traced suggests that the latter case (i.e., a north-south bias) may be more likely, although this is based on the assumption that the expected azimuth distribution is uniform in the 0° – 90° range (Figure 4.4). Moreover, planetary surface processes have deformed crater morphologies over time (Weiss, 2019), although it is not clear whether this means the azimuths retrieved were as a result systematically biased. Further caveats about the impactor model also apply, including uncertainties in the inclination bias of simulated impactors, specifically that the decision to include Hungaria group asteroids, which are high-inclination and possibly not stable over the \sim 3 Ga history simulated, may have positively biased the inclination of impactors (Bottke et al., 2002, 2012; Cuk, 2012; JeongAhn & Malhotra, 2015; Cuk & Nesvorný, 2017). However, the effect of this is likely minimal because, as Holo et al. (2018) point out, only one Hungaria asteroid was included in the 124 close encounters.

Jakosky (2021) argued, based on Schultz & Lutz-Garihan (1982), that elliptic impact craters on Mars may not be a reliable signal of actual past bolide activity in relation to obliquity, a possibility that casts doubt on the reliability of Holo et al. (2018)'s technique. Schultz & Lutz-Garihan (1982) had observed that Mars exhibits an unusually large number of elliptic craters compared to the Moon and Mercury and, based on their additional observation that many such craters appeared along great circles, argued that these resulted from impacts by Mars satellites whose orbits had tidally decayed. According to Kite (pers. comm., April 17, 2022), however, the predictions of earlier approaches, such as those of Schultz & Lutz-Garihan (1982), have not been borne out by new evidence in the form of large crater databases: for instance, Robbins & Hynek (2012)'s database does not in fact show a collimation of craters in the form of a great circle.

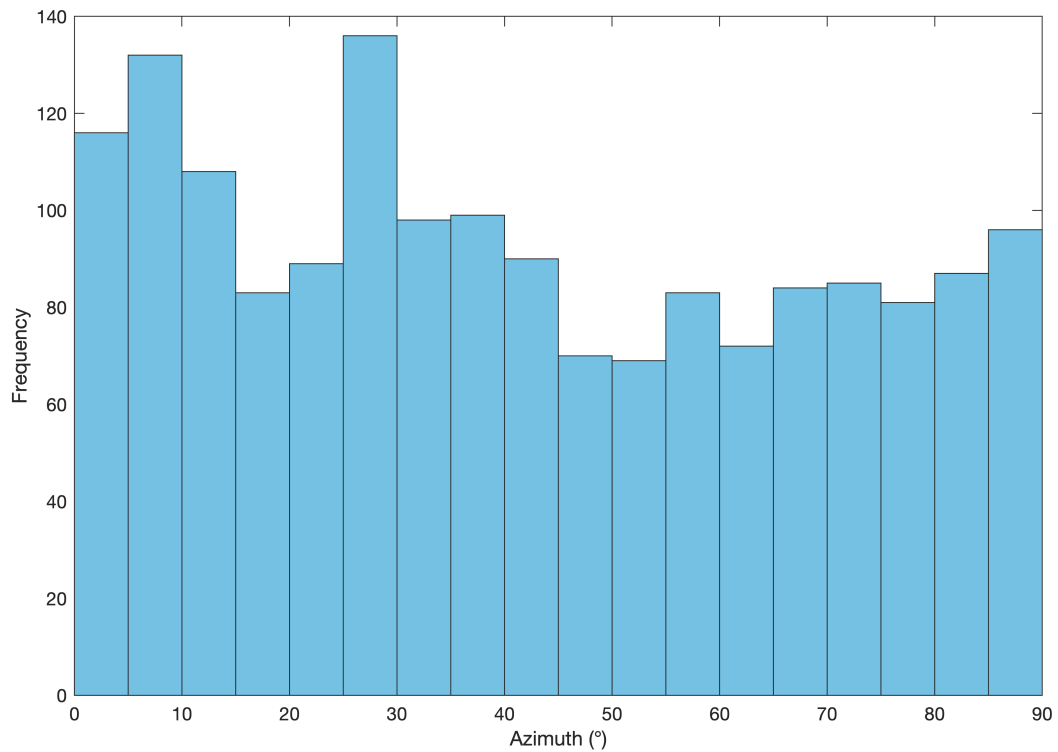


Figure 4.4: Frequency histogram of number of elliptic craters traced per 5° azimuth bin for both the lAv and AHv units.

5 CONCLUSION

Given that Mars obliquity oscillates chaotically over >100 Ma time scales, constraining its historical path requires the careful use of statistical analysis and geologic evidence. Using the impact cratering forward-model developed by Holo et al. (2018), and gathering fresh geologic evidence in the form of 1,678 elliptic crater traces on two geologic units of different ages (the lAv unit and AHv unit), we attempted to constrain the mean obliquity of Mars over the past ~ 0.9 Ga and the past ~ 2.0 Ga, finding that they were 66° (56.2° – 74.6° standard deviation interval) and 8° (0.0° – 14.4° standard deviation interval) respectively. Our procedure comprised first generating azimuth distributions of simulated craters under different obliquity scenarios, then normalizing those craters for the relevant latitude distributions associated with the sampled areas, and finally performing χ^2 tests to measure the extent of mismatch between the simulated data from each obliquity scenario and the real observations. This result, if correct, implies that Mars, during its high-obliquity recent (past ~ 0.9 Ga) past, saw greater water-ice sublimation, water-ice migration to the middle- and low latitudes, higher water vapor pressure, and more frequent polar dust storms; and, during its low-obliquity further (past ~ 2.0 Ga) past, saw extensive polar glaciation, polar atmospheric collapse, and deep aquifer desiccation.

Our interpretation of these results considers several factors. First, our results are only partially congruent with those of Holo et al. (2018). On the one hand, the low mean obliquity over the past ~ 2.0 Ga is compatible with their mean obliquity estimate for the past ~ 3.5 Ga, between $\sim 10^\circ$ and $\sim 30^\circ$. On the other hand, however, the fraction of time spent at high obliquity, per this study's results, most likely exceeds the one-fifth estimate. Second, implementing a procedure that considers inter-analyst error moderates the mean obliquity estimates to (in our median result) 63° (54.7° – 72.0° standard deviation interval) and 14° (6.3° – 20.5° standard deviation interval), respectively, and is likely required for our results to be internally compatible. Third, various limitations including the small number of elliptic

621 craters, failure to check for poke-through older craters and caveats about Holo et al. (2018)'s
622 pipeline require that further investigation continue to probe the past obliquity of Mars. Fur-
623 ther research can continue with the present method by amassing a more comprehensive set
624 of craters and quantifying the errors caused by poke-throughs of older craters on younger
625 terrain. Adopting a more critical lens, future work should cross-check this study's methods
626 with Holo et al. (2018)'s by applying it to Holo et al. (2018)'s dataset and vice versa and
627 re-evaluate the study's unphysical result for the intervening \sim 1.06 Ga period between the
628 ages of the units.

629

REFERENCES

- 630 Abe, Y., Numaguti, A., Komatsu, G., & Kobayashi, Y. (2005). Four climate regimes on
 631 a land planet with wet surface: Effects of obliquity change and implications for ancient
 632 Mars. *Icarus*, 178(1), 27–39. <https://doi.org/10.1016/j.icarus.2005.03.009>
- 633 Adeli, S., Hauber, E., Michael, G., Fawdon, P., Smith, I., & Jaumann, R. (2019). Geomor-
 634 phological evidence of localized stagnant ice deposits in Terra Cimmeria, Mars. *Jour-*
 635 *nal of Geophysical Research: Planets*, 124(6), 1525–1541. <https://doi.org/10.1029/2018je005772>
- 637 Bills, B. (1999). Obliquity-oblateness feedback on Mars. *Journal of Geophysical Research: Planets*, 104(E12), 30773–30797. <https://doi.org/10.1029/1999je001057>
- 639 Bills, B., & Keane, J. (2019). Mars obliquity variations are both non-chaotic and possibly
 640 fully damped. In *Lunar and Planetary Institute Contributions*, 2132. The Woodlands,
 641 Texas: 50th Lunar and Planetary Science Conference. <https://ui.adsabs.harvard.edu/abs/2019LPI....50.3276B>
- 643 Bottke, W., Love, S., Tytell, D., & Glotch, T. (2000). Interpreting the elliptical crater
 644 populations on Mars, Venus, and the Moon. *Icarus*, 145(1), 108–121. <https://doi.org/10.1006/icar.1999.6323>
- 646 Bottke, W., Morbidelli, A., Jedicke, R., Petit, J.-M., Levison, H., Michel, P., & Metcalfe, T.
 647 (2002). Debiased orbital and absolute magnitude distribution of the near-Earth objects.
 648 *Icarus*, 156(2), 399–433. <https://doi.org/10.1006/icar.2001.6788>
- 649 Bottke, W., Vokrouhlický, D., Minton, D., Nesvorný, D., Morbidelli, A., Brasser, R., Simon-
 650 son, B., & Levison, H. (2012). An Archaean heavy bombardment from a destabilized
 651 extension of the asteroid belt. *Nature*, 485(7396), 78–81. <https://doi.org/10.1038/nature10967>
- 653 Bretagnon, P. (1974). Termes à longues périodes dans le système solaire. *Astronomy and Astrophysics*, 30(1), 141–154. <https://ui.adsabs.harvard.edu/abs/1974A&A....30..141B>
- 656 Brouwer, D., & van Woerkom, A. (1950). The secular variations of the orbital elements of the
 657 principal planets. *Astronomical Papers Prepared for the Use of the American Ephemeris and Nautical Almanac*, 13, 81–107. <https://ui.adsabs.harvard.edu/abs/1950USNAO..13...81B>
- 660 Buhler, P., & Piqueux, S. (2021). Obliquity-driven CO₂ exchange between Mars' atmosphere,
 661 regolith, and polar cap. *Journal of Geophysical Research: Planets*, 126(5), 2020 006759.
 662 <https://doi.org/10.1029/2020je006759>
- 663 Christensen, P., Engle, E., Anwar, S., Dickenshied, S., Noss, D., Gorelick, N., & Weiss-
 664 Malik, M. (2009). JMARS - a planetary GIS. *American Geophysical Union, IN22A – 06.*
 665 <http://adsabs.harvard.edu/abs/2009AGUFMIN22A..06C>

- 666 Cuk, M. (2012). Chronology and sources of lunar impact bombardment. *Icarus*, 218, 69–79.
667 <https://doi.org/10.1016/j.icarus.2011.11.031>
- 668 Cuk, M., & Nesvorný, D. (2017). Planetary chaos and the (in)stability of Hungaria asteroids.
669 *Icarus*, 304, 9–13. <https://doi.org/10.1016/j.icarus.2017.04.015>
- 670 Dickson, J., Head, J., & Marchant, D. (2008). Late Amazonian glaciation at the dichotomy
671 boundary on Mars: Evidence for glacial thickness maxima and multiple glacial phases.
672 *Geology*, 36(5), 411–414. <https://doi.org/10.1130/g24382a.1>
- 673 Emmett, J., Murphy, J., & Kahre, M. (2020). Obliquity dependence of the formation of
674 the Martian polar layered deposits. *Planetary and Space Science*, 193, 105047. <https://doi.org/10.1016/j.pss.2020.105047>
- 676 Fassett, C., Levy, J., Dickson, J., & Head, J. (2014). An extended period of episodic north-
677 ern mid-latitude glaciation on Mars during the middle to late Amazonian: Implications
678 for long-term obliquity history. *Geology*, 42(9), 763–766. <https://doi.org/10.1130/g35798.1>
- 680 Folkner, W., Yoder, C., Yuan, D., Standish, E., & Preston, R. (1997). Interior structure
681 and seasonal mass redistribution of Mars from radio tracking of Mars Pathfinder. *Science*,
682 278(5344), 1749–1752. <https://doi.org/10.1126/science.278.5344.1749>
- 683 Forget, F., Byrne, S., Head, J., Mischna, M., & Schörghofer, N. (2017). Recent climate
684 variations. In R. Haberle, R. Clancy, F. Forget, M. Smith, & R. Zurek (Eds.) *The
685 Atmosphere and Climate of Mars*, (pp. 497–525). Cambridge University Press. <https://doi.org/10.1017/9781139060172.016>
- 687 Forget, F., Haberle, R., Montmessin, F., Levrard, B., & Head, J. (2006). Formation of
688 glaciers on Mars by atmospheric precipitation at high obliquity. *Science*, 311(5759), 368–
689 371. <https://doi.org/10.1126/science.1120335>
- 690 Gal, O. (2003). fit_ellipse. Retrieved from https://www.mathworks.com/matlabcentral/fileexchange/3215-fit_ellipse
- 692 Grimm, R., Harrison, K., Stillman, D., & Kirchoff, M. (2017). On the secular retention of
693 ground water and ice on Mars. *Journal of Geophysical Research. Planets*, 122(1), 94–109.
694 <https://doi.org/10.1002/2016je005132>
- 695 Haberle, R., & Jakosky, B. (1990). Sublimation and transport of water from the north
696 residual polar cap on Mars. *Journal of Geophysical Research*, 95(B2), 1423–1437. <https://doi.org/10.1029/jb095ib02p01423>
- 698 Haberle, R., Murphy, J., & Schaeffer, J. (2003). Orbital change experiments with a
699 Mars general circulation model. *Icarus*, 161(1), 66–89. [https://doi.org/10.1016/s0019-1035\(02\)00017-9](https://doi.org/10.1016/s0019-1035(02)00017-9)

- 701 Hartmann, W. (2005). Martian cratering 8: Isochron refinement and the chronology of Mars.
702 *Icarus*, 174, 294–320. <https://doi.org/10.1016/j.icarus.2004.11.023>
- 703 Head, J., & Marchant, D. (2003). Cold-based mountain glaciers on Mars: Western
704 Arsia Mons. *Geology*, 31(7), 641–644. [https://doi.org/10.1130/0091-7613\(2003\)031<0641:cmgomw>2.0.co;2](https://doi.org/10.1130/0091-7613(2003)031<0641:cmgomw>2.0.co;2)
- 705
- 706 Head, J., Mustard, J., Kreslavsky, M., Milliken, R., & Marchant, D. (2003). Recent ice ages
707 on Mars. *Nature*, 426(6968), 797–802. <https://doi.org/10.1038/nature02114>
- 708 Holo, S., Kite, E., & Robbins, S. (2018). Mars obliquity history constrained by elliptic crater
709 orientations. *Earth and Planetary Science Letters*, 496, 206–214. <https://doi.org/10.1016/j.epsl.2018.05.046>
- 710
- 711 Jakosky, B. (2021). Atmospheric loss to space and the history of water on Mars. *Annual
712 Review of Earth and Planetary Sciences*, 49(1), 71–93. <https://doi.org/10.1146/annurev-earth-062420-052845>
- 712
- 713
- 714 Jakosky, B., & Carr, M. (1985). Possible precipitation of ice at low latitudes of Mars dur-
715 ing periods of high obliquity. *Nature*, 315(6020), 559–561. <https://doi.org/10.1038/315559a0>
- 715
- 716
- 717 Jakosky, B., Henderson, B., & Mellon, M. (1995). Chaotic obliquity and the nature of the
718 Martian climate. *Journal of Geophysical Research*, 100(E1), 1579–1584. <https://doi.org/10.1029/94je02801>
- 718
- 719
- 720 Jawin, E., Head, J., & Marchant, D. (2018). Transient post-glacial processes on Mars:
721 Geomorphologic evidence for a paraglacial period. *Icarus*, 309, 187–206. <https://doi.org/10.1016/j.icarus.2018.01.026>
- 721
- 722
- 723 JeongAhn, Y., & Malhotra, R. (2015). The current impact flux on Mars and its seasonal
724 variation. *Icarus*, 262, 140–153. <https://doi.org/10.1016/j.icarus.2015.08.032>
- 724
- 725 Kent, D., Olsen, P., Rasmussen, C., Lepre, C., Mundil, R., Irmis, R., Gehrels, G., Giesler,
726 D., Geissman, J., & Parker, W. (2018). Empirical evidence for stability of the 405-kiloyear
727 Jupiter–Venus eccentricity cycle over hundreds of millions of years. *Proceedings of the
728 National Academy of Sciences*, 115(24), 6153–6158. <https://doi.org/10.1073/pnas.1800891115>
- 728
- 729
- 730 Kite, E., Howard, A., Lucas, A., Armstrong, J., Aharonson, O., & Lamb, M. (2015). Stratig-
731 raphy of Aeolis Dorsa, Mars: Stratigraphic context of the great river deposits. *Icarus*, 253,
732 223–242. <https://doi.org/10.1016/j.icarus.2015.03.007>
- 732
- 733 Kreslavsky, M., & Head, J. (2005). Mars at very low obliquity: Atmospheric collapse and
734 the fate of volatiles. *Geophysical Research Letters*, 32(12), 12202. <https://doi.org/10.1029/2005gl1022645>
- 734
- 735

- 736 Kreslavsky, M., & Head, J. (2011). Carbon dioxide glaciers on Mars: Products of recent low
737 obliquity epochs (?). *Icarus*, 216(1), 111–115. <https://doi.org/10.1016/j.icarus.2011.08.020>
- 739 Laskar, J. (1988). Secular evolution of the solar system over 10 million years. *Astronomy and Astrophysics*, 198, 341–362. <https://ui.adsabs.harvard.edu/abs/1988A&A..198..341L>
- 742 Laskar, J., Correia, A., Gastineau, M., Joutel, F., Levrard, B., & Robutel, P. (2004). Long
743 term evolution and chaotic diffusion of the insolation quantities of Mars. *Icarus*, 170(2),
744 343–364. <https://doi.org/10.1016/j.icarus.2004.04.005>
- 745 Laskar, J., Gastineau, M., & Joutel, F. (2010). Astronomical solutions for Martian paleo-
746 climates [Data set]. Astronomie et systèmes dynamiques, Institut de mécanique céleste.
747 Retrieved from <http://vo.imcce.fr/insola/earth/online/mars/mars.html>
- 748 Laskar, J., & Robutel, P. (1993). The chaotic obliquity of the planets. *Nature*, 361(6413),
749 608–612. <https://doi.org/10.1038/361608a0>
- 750 Le Feuvre, M., & Wieczorek, M. (2008). Nonuniform cratering of the terrestrial planets.
751 *Icarus*, 197, 291–306. <https://doi.org/10.1016/j.icarus.2008.04.011>
- 752 Leighton, R., & Murray, B. (1966). Behavior of carbon dioxide and other volatiles on Mars.
753 *Science*, 153(3732), 136–144. <https://doi.org/10.1126/science.153.3732.136>
- 754 Lindner, B., & Jakosky, B. (1985). Martian atmospheric photochemistry and composition
755 during periods of low obliquity. *Journal of Geophysical Research*, 90(A4), 3435–3440.
756 <https://doi.org/10.1029/ja090ia04p03435>
- 757 Ma, C., Meyers, S., & Sageman, B. (2017). Theory of chaotic orbital variations confirmed
758 by Cretaceous geological evidence. *Nature*, 542(7642), 468–470. <https://doi.org/10.1038/nature21402>
- 760 Madeleine, J.-B., Forget, F., Head, J., Levrard, B., Montmessin, F., & Millour, E. (2009).
761 Amazonian northern mid-latitude glaciation on Mars: A proposed climate scenario. *Icarus*,
762 203(2), 390–405. <https://doi.org/10.1016/j.icarus.2009.04.037>
- 763 Manning, C., Bierson, C., Putzig, N., & McKay, C. (2019). The formation and stability of
764 buried polar CO₂ deposits on Mars. *Icarus*, 317, 509–517. <https://doi.org/10.1016/j.icarus.2018.07.021>
- 766 Mansfield, M., Kite, E., & Mischna, M. (2018). Effect of Mars atmospheric loss on snow melt
767 potential in a 3.5 Gyr Mars climate evolution model. *Journal of Geophysical Research: Planets*,
768 123(4), 794–806. <https://doi.org/10.1002/2017je005422>
- 769 MATLAB (2022). 9.12.0.1884302 (R2022a). Natick, Massachusetts: The MathWorks Inc.

- 770 Mau, M., Kent, D., & Clemmensen, L. (2022). Planetary chaos and inverted climate phasing
771 in the late Triassic of Greenland. *Proceedings of the National Academy of Sciences*, 119,
772 e2118696119. <https://doi.org/10.1073/pnas.2118696119>
- 773 Michael, G. (2013). Planetary surface dating from crater size-frequency distribution mea-
774 surements: Multiple resurfacing episodes and differential isochron fitting. *Icarus*, 226,
775 885–890. <https://doi.org/10.1016/j.icarus.2013.07.004>
- 776 Milkovich, S., Head, J., & Marchant, D. (2006). Debris-covered piedmont glaciers along the
777 northwest flank of the Olympus Mons scarp: Evidence for low-latitude ice accumulation
778 during the late Amazonian of Mars. *Icarus*, 181(2), 388–407. <https://doi.org/10.1016/j.icarus.2005.12.006>
- 780 Mischna, M., Baker, V., Milliken, R., Richardson, M., & Lee, C. (2013). Effects of obliquity
781 and water vapor/trace gas greenhouses in the early Martian climate. *Journal of Geophys-
782 ical Research. Planets*, 118(3), 560–576. <https://doi.org/10.1002/jgre.20054>
- 783 Mischna, M., & Piqueux, S. (2020). The role of atmospheric pressure on Mars surface
784 properties and early Mars climate modeling. *Icarus*, 342, 113496. <https://doi.org/10.1016/j.icarus.2019.113496>
- 786 Murray, B., Ward, W., & Yeung, S. (1973). Periodic insolation variations on Mars. *Science*,
787 180(4086), 638–640. <https://doi.org/10.1126/science.180.4086.638>
- 788 Mustard, J., Cooper, C., & Rifkin, M. (2001). Evidence for recent climate change on Mars
789 from the identification of youthful near-surface ground ice. *Nature*, 412(6845), 411–414.
790 <https://doi.org/10.1038/35086515>
- 791 Olsen, P., Laskar, J., Kent, D., Kinney, S., Reynolds, D., Sha, J., & Whiteside, J.
792 (2019). Mapping Solar System chaos with the Geological Orrery. *Proceedings of the
793 National Academy of Sciences*, 116(22), 10664–10673. <https://doi.org/10.1073/pnas.1813901116>
- 795 Phillips, R., Davis, B., Tanaka, K., Byrne, S., Mellon, M., Putzig, N., Haberle, R., Kahre,
796 M., Campbell, B., Carter, L., Smith, I., Holt, J., Smrekar, S., Nunes, D., Plaut, J., Egan,
797 A., Titus, T., & Seu, R. (2011). Massive CO₂ ice deposits sequestered in the south
798 polar layered deposits of Mars. *Science*, 332(6031), 838–841. <https://doi.org/10.1126/science.1203091>
- 800 Robbins, S., & Hynek, B. (2012). A new global database of Mars impact craters ≥ 1 km: 1.
801 database creation, properties, and parameters. *Journal of Geophysical Research*, 117(E5),
802 05004. <https://doi.org/10.1029/2011je003966>
- 803 Root, M., & Elwood Madden, M. (2012). Potential effects of obliquity change on gas hydrate
804 stability zones on Mars. *Icarus*, 218(1), 534–544. <https://doi.org/10.1016/j.icarus.2011.12.024>

- 806 Rubincam, D. (1993). The obliquity of Mars and “climate friction”. *Journal of Geophysical*
807 *Research*, 98(E6), 10827. <https://doi.org/10.1029/93je00999>
- 808 Rubincam, D. (1999). Mars secular obliquity change due to water ice caps. *Journal of Geo-*
809 *physical Research*, 104(E12), 30765–30771. <https://doi.org/10.1029/1999je001045>
- 810 Sageman, B., Singer, B., Meyers, S., Siewert, S., Walaszczyk, I., Condon, D., Jicha, B.,
811 Obradovich, J., & Sawyer, D. (2014). Integrating $^{40}\text{Ar}/^{39}\text{Ar}$, U–Pb, and astronomical
812 clocks in the Cretaceous Niobrara Formation, Western Interior Basin, USA. *Geological*
813 *Society of America Bulletin*, 126(7/8), 956–973. <https://doi.org/10.1130/b30929.1>
- 814 Schultz, P., & Lutz-Garihan, A. (1982). Grazing impacts on Mars: A record of lost satel-
815 *lites*. *Journal of Geophysical Research*, 87(S01), 84–96. <https://doi.org/10.1029/jb087is01p00a84>
- 817 Schwarz, D. (2017). Fast and robust curve intersections. Retrieved
818 from <https://www.mathworks.com/matlabcentral/fileexchange/11837-fast-and-robust-curve-intersections>
- 820 Segschneider, J., Grieger, B., Keller, H., Lunkeit, F., Kirk, E., Fraedrich, K., Rodin, A., &
821 Greve, R. (2005). Response of the intermediate complexity Mars Climate Simulator to
822 different obliquity angles. *Planetary and Space Science*, 53(6), 659–670. <https://doi.org/10.1016/j.pss.2004.10.003>
- 824 Shean, D., Head, J., III, Fastook, J., & Marchant, D. (2007). Recent glaciation at high
825 elevations on Arsia Mons, Mars: Implications for the formation and evolution of large
826 tropical mountain glaciers. *Journal of Geophysical Research*, 112(E3), 03004. <https://doi.org/10.1029/2006je002761>
- 828 Shoelson, B. (2012). Patchline. Retrieved from <https://www.mathworks.com/matlabcentral/fileexchange/36953-patchline>
- 830 Soto, A., Mischna, M., Schneider, T., Lee, C., & Richardson, M. (2015). Martian atmospheric
831 collapse: Idealized GCM studies. *Icarus*, 250, 553–569. <https://doi.org/10.1016/j.icarus.2014.11.028>
- 833 Tanaka, K., Skinner, J., Jr., Dohm, J., Irwin, R., III, Kolb, E., Fortezzo, C., Platz, T.,
834 Michael, G., & Hare, T. (2014). Geologic map of Mars. *U.S. Geological Survey Scien-*
835 *tific Investigations Map*, 3292, Scale 1:20,000,000, Pamphlet 43 p. <https://doi.org/10.3133/sim3292>
- 837 Touma, J., & Wisdom, J. (1993). The chaotic obliquity of Mars. *Science*, 259(5099), 1294–
838 1297. <https://doi.org/10.1126/science.259.5099.1294>
- 839 Ward, W. (1973). Large-scale variations in the obliquity of Mars. *Science*, 181(4096), 260–
840 262. <https://doi.org/10.1126/science.181.4096.260>

- 841 Ward, W. (1974). Climatic variations on Mars: 1. astronomical theory of insola-
842 tion. *Journal of Geophysical Research*, 79(24), 3375–3386. <https://doi.org/10.1029/jc079i024p03375>
- 844 Ward, W. (1979). Present obliquity oscillations of Mars: Fourth-order accuracy in orbital e
845 and I . *Journal of Geophysical Research*, 84(B1), 237–241. <https://doi.org/10.1029/jb084ib01p00237>
- 847 Ward, W. (1992). Long-term orbital and spin dynamics of Mars. In H. Kieffer, B. Jakosky,
848 C. Snyder, & M. Matthews (Eds.) *Mars*, (pp. 298–320). University of Arizona Press.
849 <https://doi.org/10.2307/j.ctt207g59v.13>
- 850 Ward, W., Burns, J., & Toom, O. (1979). Past obliquity oscillations of Mars: The role of the
851 Tharsis uplift. *Journal of Geophysical Research*, 84(B1), 243–259. <https://doi.org/10.1029/jb084ib01p00243>
- 853 Ward, W., & Rudy, D. (1991). Resonant obliquity of Mars? *Icarus*, 94(1), 160–164. [https://doi.org/10.1016/0019-1035\(91\)90146-k](https://doi.org/10.1016/0019-1035(91)90146-k)
- 855 Weiss, D. (2019). Mars in ice ages for \sim 25% of post-Noachian geologic history. *Earth*
856 and *Planetary Science Letters*, 528, 115847. <https://doi.org/10.1016/j.epsl.2019.115847>
- 858 Weiss, D., & Head, J. (2015). Crater degradation in the Noachian highlands of Mars: As-
859 sessing the hypothesis of regional snow and ice deposits on a cold and icy early Mars.
860 *Planetary Space Science*, 117, 401–420. <https://doi.org/10.1016/j.pss.2015.08.009>
- 861 Yoder, C., & Standish, E. (1997). Martian precession and rotation from Viking lander range
862 data. *Journal of Geophysical Research: Planets*, 102(E2), 4065–4080. <https://doi.org/10.1029/96je03642>
- 864 Zent, A. (2013). Orbital drivers of climate change on Earth and Mars. In S. Mackwell,
865 A. Simon-Miller, J. Harder, & M. Bullock (Eds.) *Comparative Climatology of Terrestrial*
866 *Planets*, (pp. 505–538). University of Arizona Press. https://doi.org/10.2458/azu_uapress_9780816530595-ch21

APPENDIX: CODE

A.1 hu_01_get_crater_data.m

```

%% ***** STEP 01 *****
% Read crater coordinate data from shapefiles and trace ellipses using
% Gal (2003)'s script. Export data as in five columns (latitude, azimuth,
% diameter, ellipticity, longitude).
%
% *****

for option = 1:3
    if option == 1
        shapefile = 'traces/lAv.shp';
    elseif option == 2
        shapefile = 'traces/AHv.shp';
    elseif option == 3
        shapefile = 'traces/RetraceKite.shp';
    end

    S = shaperead(shapefile);

    a = zeros(length(S),4);
    R = 3389.5;
    digits(32);

    for i = 1:length(S)

```

```

long = S(i).X;
lat = S(i).Y;

long = long(~isnan(long));
lat = lat(~isnan(lat));

cen_long = fit_ellipse(long,lat).X0_in;

if isempty(cen_long)
    a(i,:) = [NaN,NaN,NaN,NaN,NaN];
    continue;
else
    ellipse = fit_ellipse((long-cen_long).*cosd(lat)+cen_long,lat);
    if isempty(ellipse.status)
        % Latitude
        a(i,1) = ellipse.Y0_in;
        % Azimuth
        a(i,2) = 90-abs(rad2deg(ellipse.phi));
        % Diameter
        a(i,3) = 2*sqrt(2*pi*R/360*0.5*ellipse.long_axis...
            *2*pi*R/360*0.5*ellipse.short_axis);
        % Ellipticity
        a(i,4) = ellipse.long_axis/ellipse.short_axis;
        % Longitude
        a(i,5) = ellipse.X0_in;
    else

```

```

    a(i,:) = [NaN,NaN,NaN,NaN,NaN];
end
end
end

% Filter for craters with ellipticity > e_crit
for e_crit = 1:0.05:1.15
    if e_crit > 1
        a = a(a(:,4) >= e_crit,:);
    end

    if option == 1
        fname = sprintf('craters_obs/lAv%.2f.mat', e_crit);
        save(fname,'a')
    elseif option == 2
        fname = sprintf('craters_obs/AHv%.2f.mat', e_crit);
        save(fname,'a')
    elseif option == 3
        fname = sprintf('craters_obs/RetraceKite%.2f.mat', e_crit);
        save(fname,'a')
    end
end
end

% Filter for craters with ellipticity > e_crit
load('craters_obs/TraceHolo1.00.mat')

```

```

for e_crit = 1.05:0.05:1.15
    a = a(a(:,4) >= e_crit,:);
    fname = sprintf('craters_obs/TraceHolo%.2f.mat', e_crit);
    save(fname, 'a')
end

```

870

A.2 hu_02_get_azimuth_diffs.m

```

%% ***** STEP 02 *****
% Identify the coordinates of second analyst's traced craters; generate
% list of craters in original traced set that are close to those in second;
% if there are multiple craters in this list choose the one with the
% highest resemblance; check how different the craters are in terms of
% azimuth (add this to an array); make an array with crater azimuth
% difference.
%
```

James Hu, 2022

```

e_crit = 1.05;

for mode = 1:2
    if mode == 1
        load(sprintf('craters_obs/RetraceKite%.2f.mat',e_crit), 'a')
    elseif mode == 2
        load(sprintf('craters_obs/TraceHolo%.2f.mat',e_crit), 'a')
    end

```

```

b = a;

load(sprintf('craters_obs/lAv%.2f.mat',e_crit))

lAv = a;

load(sprintf('craters_obs/AHv%.2f.mat',e_crit))

AHv = a;

a = cat(1,lAv,AHv);

x = 0.1;

y = 0.1;

a1 = zeros(size(b));

for i = 1:length(b)

a0 = a(abs(a(:,1) - b(i,1)) <= x & abs(a(:,5) - b(i,5)) <= x & ...

abs(a(:,3) - b(i,3)) <= y, ...

:);

if isempty(a0)

    disp('Analog not found for crater.');

elseif height(a0) > 1

    disp('Multiple analogs found.');

else

    disp('Unique analog found. ');

    a1(i,:) = a0;

```

```

    end

end

% Find diffs
azimuth_diff = a1(:,2) - b(:,2);

% Filter for where unique analog found
azimuth_diff = azimuth_diff(find(a1(:,2)),:);

% Duplicate and get opposite diffs
azimuth_diff = cat(1,azimuth_diff,azimuth_diff.*-1);

% Export
if mode == 1

    fname = sprintf('iaerr_perts/iaerr_Kite%.2f.mat', e_crit);
    save(fname,'azimuth_diff')

elseif mode == 2

    fname = sprintf('iaerr_perts/iaerr_Holo%.2f.mat', e_crit);
    save(fname,'azimuth_diff')

end

end

```

871

A.3 hu_03_get_pois.m

```

%% ***** STEP 03 *****
% This is the first script in Sam Holo's forward model for the effect of
% obliquity on elliptic crater orientations. The input file is name

```

```
% '14mag_imp_info' and contains an ensemble of encounter inclinations and  
% speeds from n-body output. The output of this script is an ensemble of  
% elliptic crater locations and diameters, as well as impactor velocity  
% vectors at the time of impact and the impact angle. This output can be  
% ingested and processed by apply_obliquity.m.
```

```
%
```

Sam Holo, 2018

```
% *****
```

```
% Set variables for physical constants
```

```
G = 6.67408e-11;
```

```
R = 3.3895e6;
```

```
M = 6.4171e23;
```

```
vesc = 5027;
```

```
g = 3.71;
```

```
% Load impact info file - This needs two values: encounter
```

```
% inclinations and speeds from n-body output
```

```
load('forward_model/14mag_imp_info.mat','inclinations','speeds');
```

```
% Set parameters for the size frequency distribution
```

```
% NOTE: the SFD parameters have been tuned for a particular impactor
```

```
% population, this will NOT immediately translate to different populations
```

```
lmin = 21;
```

```
alpha = 0.65;
```

```
n = 1e6;
```

```

% Pre-assign random numbers and place for impact info

[speeds,id] = datasample(speeds,n);

inclinations = inclinations(id);

impactinfo = zeros(n,9);

randos = rand(n,4);

% Loop through each of the seeded inclination-speed pairs

for i = 1:n

    % set the impact parameters

    speed = speeds(i);

    tau = R*sqrt(1 + (2*G*M)/(R*speed*speed));

    inc = inclinations(i);

    % Sample from our assumed SFD and apply crater diameter scaling prior
    % to correction for impact angle

    prob = randos(i,4);

    imp_diam = lmin*(prob)^(1/(-1*alpha)); impdiamstore(i) = imp_diam;

    d90 = 1.161*(g^(-0.22))*(speed^(0.44))*(imp_diam^(0.78));

    % Calculate the critical angle from cratering efficiency

    % Later we will "flag" if the generated crater is elliptical or not

    theta_c = 45*(d90/imp_diam)^(-0.52) + 77*(d90/imp_diam)^(-1.85);

    % Here we create impacts with angles < 45 degrees

    bsq = (tau^2)*(0.5 + 0.5*randos(i,1));

```

```

b = sqrt(bsq);
theta = acos(b/tau);
del = randos(i,2)*2*pi;
phi = randos(i,3)*2*pi;

% Semi major axis of hyperbolic orbit
a = G*M/(speed^2);

% Eccentricity
ecc = sqrt(1 + (b^2)*(speed^4)/ ((G^2)*(M^2)) );

% Cosine and sine of true anomaly at launch point
cinf = -1/ecc;
sinf = -1*sqrt(1 - (cinf^2));

% Cosine and sine of true anomaly at impact
cimp = (((a/R)*(ecc^2 - 1))-1)/ecc;
simp = -1*sqrt(1 - (cimp^2));

% Calculate impact location in projectile coordinates
yi = -R*(cimp*cinf + simp*sinf);
xi = R*(simp*cinf - cimp*sinf);
zi = 0;
pos = [xi;yi;zi];
rotangle = pi/2 + theta;

```

```

% Calculate impact velocities from momentum conservation

speed = sqrt((speed)^2 + vesc^2);
vimp = speed*[cos(rotangle), -1*sin(rotangle), 0; sin(rotangle), ...
    cos(rotangle), 0; 0, 0, 1]*pos/norm(pos);

% Rotatation matrix for the effect of impact argument

cd = cos(del);
sd = sin(del);
Mdel = [cd, 0, -1*sd; 0, 1, 0; sd, 0, cd];

% Rotatation matrix for the effect of impactor inclination

ci = cos(inc);
si = sin(inc);
Minc = [1, 0, 0; 0, ci, si; 0, -1*si, ci];

% Rotatation matrix for the effect of randomized precessional season

sphi = sin(phi);
cphi = cos(phi);
Mprec = [cphi, -1*sphi, 0; sphi, cphi, 0; 0, 0, 1];

% Update position and velocity by applying rotations

pos = (Mprec*(Minc*(Mdel*pos)));
vimp = (Mprec*(Minc*(Mdel*vimp)));

% Store position and velocity vectors, along with impact angles

impactinfo(i, 1:6) = [pos; vimp]';

```

```

impactinfo(i,7) = theta;
impactinfo(i,9) = deg2rad(theta_c);

% Correct for the effect of impact angle in crater diameter and store
crater_diam = d90*(sin(theta)^(1/3))/1000; % Remember scaling is in m!
impactinfo(i,8) = crater_diam;

end

impactinfo = impactinfo(impactinfo(:,7) < impactinfo(:,9),:);

% Save the data

newfile = 'forward_model/14mag_pois.mat';
save(newfile,'impactinfo',' -v7.3');

```

872

A.4 hu_04_apply_obliquity.m

```

%% ***** STEP 04 *****
% This is the second script in Sam Holo's forward model for the effect of
% obliquity on elliptic crater orientations. It takes the output ensemble
% from get_pois.m (get "pre-obliquity-impacts"), applies each integer
% degree obliquity to the ensemble, and saves the key parameters: latitude,
% diameter, and orientation of the elliptic craters.

%
% *****

% Load the impact data from get_pois.m
load('forward_model/14mag_pois.mat','impactinfo');

```

```

% Set the diameter (in km) below which you throw out model craters
diam_cutoff = 4;

% Filter out craters that are too small for the analysis
R = 3.3895e6;
impactinfo = impactinfo(impactinfo(:,8)>= diam_cutoff,:);
len = length(impactinfo);

% Pre-allocate space for the centers/counts of the model output
latdata = zeros(len,91);
orientationdata = zeros(len,91);
diamdata = zeros(len,91);

% Loop through the possible values for obliquity
for i = 0:90
    % Set the obliquity NOTE: here we are working in degrees
    obl = i;

    % Loop through each elliptic-crater producing impact
    for j = 1:len
        % Define the obliquity rotation matrix
        cobl = cosd(obl);
        sobl = sind(obl);
        Mobl = [1,0,0;0,cobl,sobl;0,-1*sobl,cobl];

```

```

% Apply the obliquity rotation to the position and velocity vectors

pos = Mobj*impactinfo(j,1:3)';
vimp = Mobj*impactinfo(j,4:6)';

% Calculate latitude

latdata(j,i+1) = abs(asind(pos(3)/norm(pos))) ;

% Calculate the impact orientation by projecting northbound and
% velocity vectors onto the planet's tangent plane

poshat = pos/norm(pos);
north = [0;0;R] - pos;
northproj = north - dot(north,poshat)*poshat;
trajectoryproj = vimp - dot(vimp,poshat)*poshat;

if norm(northproj) ~= 0
    northproj = northproj/norm(northproj); % Normalize
end

if norm(trajectoryproj) ~= 0
    trajectoryproj = trajectoryproj/norm(trajectoryproj); % N'lize
end

azimuth = acosd(dot(northproj,trajectoryproj));
azimuth(azimuth > 90) = 180-azimuth;
orientationdata(j,i+1) = azimuth;
diamdata(j,i+1) = impactinfo(j,8);

```

```

    end
    % Display progress
    disp(i);

end

% Save the data
newfile = 'forward_model/obpreds4.mat';
save(newfile,'latdata','orientationdata','diamdata');

```

873

A.5 hu_05_apply_lat_dist.m

```

%% ***** STEP 05 *****
% Modify the output of Sam Holo's forward model to conform to the
% latitudinal distribution of actually observed craters.

%
% *****

for e_crit = 1.00:0.05:1.15
    for mode = 1:2    % 1 = lAv; 2 = AHv
        load('forward_model/obpreds4.mat','orientationdata','latdata',...
              'diamdata');

        if mode == 1
            load(sprintf('craters_obs/lAv%.2f.mat',e_crit));
        elseif mode == 2
            load(sprintf('craters_obs/AHv%.2f.mat',e_crit));
        end
    end
end

```

```

% Fold observed latitudes by assumption of N/S hemispheric symmetry
folded_lats = abs(a(:,1));
clear a;

% Determine the empirical and simulated latitudinal distribution
emp_lat_dist = hu_05a_find_lat_dist(folded_lats);
sim_lat_dists = zeros(17,91);

for i = 0:90
    sim_lat_dists(:,i+1) = hu_05a_find_lat_dist(latdata(:,i+1));
end

% Normalize to bin with greatest simulation/empirical disparity
scale_factors = emp_lat_dist ./ sim_lat_dists;
scale_factors = scale_factors / max(scale_factors(:));

% Get indices by proportionally resampling sim craters wrt 5°
% latitude bin; note: method obtains indices before applying those
% to lats, ors, diams
size = 1e6;
idx = zeros(size,91);

for i = 0:90
    resampled = [] ;

```

```

for bin = 1:17

    latdata_at_lat = latdata(:,i+1);

    id = find(latdata_at_lat > 5*(bin-1)&...
               latdata_at_lat <= 5*(bin-1) + 5);

    sample = datasample(id,round(height(id)*...
                                scale_factors(bin,i+1)), 'Replace',...
                                false);

    resampled = cat(1,resampled,sample);

end

idx(:,i+1) = datasample(resampled,size);

end

% Apply indices to latitudes, orientations, and diameters

resampled_lats = zeros(size,91);
resampled_orientations = zeros(size,91);
resampled_diams = zeros(size,91);

% Loop through each obliquity

for i = 0:90

    lat = latdata(:,i+1);
    resampled_lats(:,i+1) = lat(idx(:,i+1));
    orientation = orientationdata(:,i+1);
    resampled_orientations(:,i+1) = orientation(idx(:,i+1));
    diam = diamdata(:,i+1);
    resampled_diams(:,i+1) = diam(idx(:,i+1));

end

```

```

% Export

latdata = resampled_lats;

orientationdata = resampled_orientations;

diamdata = resampled_diams;

if mode == 1

    fname = sprintf('forward_model/obpreds4_norm_lAv%.2f.mat', ...

        e_crit);

elseif mode == 2

    fname = sprintf('forward_model/obpreds4_norm_AHv%.2f.mat', ...

        e_crit);

end

save(fname,'latdata','orientationdata','diamdata','-v7.3');

end

end

function lat_dist = hu_05a_find_lat_dist(lats)

lat_dist = zeros(17,1);

for i = 1:17 % 5*(17-1)+5 = 90°

    freq_at_lat = height(lats(lats > 5*(i-1) & lats <= 5*(i-1) + 5)) ...

        / (height(lats)*width(lats));

    lat_dist(i) = freq_at_lat;

end

end

```

A.6 hu_06_get_mismatch.m

```
%% ***** STEP 06 *****
% Calculate the degree of mismatch (rdc chi-2 statistic) between the crater
% orientation probability distribution function of each constant-obliquity
% simulation (0-90°) and the crater orientation probability distribution
% function as determined from the actually observed craters. Then determine
% the constant obliquity with the lowest mismatch.

%
% *****

e_crit = 1.1;
num_inst = 1000; % Number of instances of inter-analyst perturbation

% 1. Load the appropriate crater data and latitude-normalized obliquity
% predictions.

scenario = 2; % 1 = constant obliquity;
                % 2 = Gaussian variation around mean obliquity

if scenario == 2
    sigma = 5.0326; % Standard deviation from Laskar 2004, past 2.5 Ma:
                    % load('laskar/laskar_nonchaotic.mat')
                    % rad2deg(std(laskar(1:2501,2)))
end

for mode = 1:2 % 1 = lAv; 2 = AHv
    if mode == 1
        load(sprintf('craters_obs/lAv%.2f.mat', e_crit))
```

```

load(sprintf('iaerr_perts/lAv%.2f_pert%d.mat',e_crit,num_inst))

load(sprintf('forward_model/obpreds4_norm_lAv%.2f.mat',e_crit),...
    'orientationdata')

elseif mode == 2

load(sprintf('craters_obs/AHv%.2f.mat',e_crit))

load(sprintf('iaerr_perts/AHv%.2f_pert%d.mat',e_crit,num_inst))

load(sprintf('forward_model/obpreds4_norm_AHv%.2f.mat',e_crit),...
    'orientationdata')

end

cratdata = a(:,2);

clear a


% 2. Take the actual crater orientations and construct crude
% probability distribution function (histogram)

bin_centers = 5:10:85;

num_bins = width(bin_centers);

[N,X] = hist(cratdata,bin_centers); % Raw frequencies

[N_p,X_p] = hist(cratdata_p,bin_centers); % Perturbed


num_crats = height(cratdata);

N_norm = N / num_crats / num_bins; % Normalized distribution

N_norm_p = N_p / num_crats / num_bins; % Perturbed

N_norm_p_median = median(N_norm_p,2);

```

```

%% Compare the PDFs of the actual and simulated crater orientations

% 3. Calculate the standard error on the actual crater probability
% distribution function; plot with error bars

fig1 = figure('color',[1 1 1]);

subplot(2,1,mode)

hold on

for i = 1:1000

    patchline(X_p,N_norm_p(:,i),'edgecolor','#74C1E4','linewidth',5, ...
        'edgealpha',0.01) % (3)Blue

end

E = sqrt(N) / num_crats / num_bins;

errorbar(X,N_norm,E,'Color','#8D6135','LineWidth',1.5) % (1)Brown
plot(X_p,N_norm_p_median,'Color','#74C1E4','LineWidth',1.5)

% 4. Take the simulated crater orientation data and construct crude
% probability distribution functions; plot

sims = zeros(91,num_bins);
num_simcrats = height(orientationdata);

for i = 0:1:90 % Loop through all obliquity scenarios

    if scenario == 1

        odata = orientationdata(:,i+1);

```

```

elseif scenario == 2

    odata = hu_06b_gaussamp(orientationdata,i,sigma);

end

f = hist(odata,bin_centers) / num_simcrats / num_bins;

sims(i+1,:) = f;

if ismember(i,15:15:75) % But only plot 15,30,45,60,75
    plot(bin_centers,f,'LineWidth',0.75,'LineStyle','--');

end

%% Conduct 91 chi-squared tests to determine best-match constant obliquity

% 5. Calculate reduced chi-squared values for each obliquity

chi2_sims = hu_06a_chi2test(sims'*num_crats*num_bins,N');

chi2_sims_p = zeros(91,1000);

for i = 1:1000

    chi2_sims_p(:,i) = hu_06a_chi2test(sims'*num_crats*num_bins, ...
                                         N_p(:,i)');

end

chi2_sims_rdc = chi2_sims / (num_bins-1);
chi2_sims_rdc_p = chi2_sims_p / (num_bins-1);

```

```

chi2_sims_rdc_p_median = median(chi2_sims_rdc_p,2);

%% 6. Plot

fig2 = figure('color',[1 1 1]);
hold on
ylim([0 25])

for i = 1:1000
    patchline(0:90,chi2_sims_rdc_p(:,i),'edgecolor','#74C1E4',...
        'linewidth',5,'edgealpha',0.01)
end

plot(0:90,chi2_sims_rdc,'LineWidth',1.5,'Color','#8D6135')

plot(0:90,chi2_sims_rdc_p_median,'LineWidth',1.5,'Color','#74C1E4')
[~,chi2_sims_rdc_p_mins] = min(chi2_sims_rdc_p);
chi2_sims_rdc_p_mins = chi2_sims_rdc_p_mins - 1;

% Code for Fig 3.3 (ingested by hu05_plot_age_obliquity.m)

if mode == 1
    fname = sprintf('iaerr_perts/chi2_sims_rdc_p_mins_lAv%.2f',e_crit);
elseif mode == 2
    fname = sprintf('iaerr_perts/chi2_sims_rdc_p_mins_AHv%.2f',e_crit);
end

save(fname,'chi2_sims_rdc_p_mins')

```

```

% 7. Draw lines on plot

[yMin_rdc,xIndex_rdc] = min(chi2_sims_rdc); % Observed

xline(xIndex_rdc-1,'Color','#8D6135','LineStyle','-','LineWidth',0.75)

y_uncert_rdc = yMin_rdc + sqrt(2*(num_bins-1))/(num_bins-1);

yline(y_uncert_rdc,'Color','#8D6135','LineStyle','--','LineWidth',0.75)

y_uncert_rdc_arr = y_uncert_rdc + zeros(1,91);

[xIndex_uncert_rdc,~] = intersections(0:90,chi2_sims_rdc,0:90, ...

y_uncert_rdc_arr);

xline([min(xIndex_uncert_rdc) max(xIndex_uncert_rdc)],'Color',...
 '#8D6135','LineStyle','--','LineWidth',0.75) % Uncertainty (x)

[yMin_rdc_p,xIndex_rdc_p] = min(chi2_sims_rdc_p_median); % Perturbed

xline(xIndex_rdc_p-1,'Color','#74C1E4','LineStyle','-','LineWidth',...
 0.75)

y_uncert_rdc_p = yMin_rdc_p + sqrt(2*(num_bins-1))/(num_bins-1);

yline(y_uncert_rdc_p,'Color','#74C1E4','LineStyle','--','LineWidth',...
 0.75)

y_uncert_rdc_arr_p = y_uncert_rdc_p + zeros(1,91);

[xIndex_uncert_rdc_p,~] = intersections(0:90,chi2_sims_rdc_p_median, ...
 0:90,y_uncert_rdc_arr_p);

xline([min(xIndex_uncert_rdc_p) max(xIndex_uncert_rdc_p)],'Color',...
 '#74C1E4','LineStyle','--','LineWidth',0.75) % Uncertainty (x)

% 8. Post-processing

```

```

clearvars -except mode scenario sigma e_crit num_inst fig*

if mode == 1
    fig11 = fig1;
    fig21 = fig2;
elseif mode == 2
    fig12 = fig1;
    fig22 = fig2;
end

clear fig1 fig2
end

%% Tile plots together

% 9. Figure 3.1

fig1 = figure;
t1 = tiledlayout(1,2,'TileSpacing','compact');

fig1a = nexttile;
copyobj(allchild(get(fig11,'CurrentAxes')),fig1a)
title('(a)')
xlim([0 90])
ylim([0.005 0.0225])

fig1b = nexttile;

```



```

    'Observed','Perturbed');

12.Orientation = 'vertical';

fig2.PaperUnits = 'centimeters';
fig2.PaperPosition = [0 0 24 16];
print(fig2,'output/fig3_2','-dpng','-r500')

function X2 = hu_06a_chi2test(observed,expected)
X2 = zeros(width(observed),1);

for i = 1:width(observed)
    for j = 1:height(observed)
        X2(i) = X2(i) + (observed(j,i) - expected(j))^2 / expected(j);
    end
end

function odata = hu_06b_gaussamp(orientationdata,i,sigma)
% Set random seed
rng('default');
rng(1);

size = height(orientationdata);

```

```

odata = zeros(size,1);

x = round(normrnd(i,sigma,round(size*2.25),1));
x_inrange = x(x >= 0 & x <= 90);
obls = x_inrange(1:size);

for k = 1:size
    odata(k) = orientationdata(k,obls(k)+1);
end
end

```

875

A.7 hu_07_plot_age_obliquity.m

```

%% ***** STEP 07 *****
% Plot the past and present obliquity of Mars, numerically integrated and
% statistically constrained, from multiple sources.

%
% *****

% 1. Load data

obl_data = [66 8];
obl_errhigh = [8.60978819 6.441972424];
obl_errlow = [9.830129137 8];

obl_pert_data = [63 14];
obl_pert_errhigh = [9.037343765 6.502919546];
obl_pert_errlow = [8.282013483 7.70412747];

```

```

load('iaerr_perts/chi2_sims_rdc_p_mins_lAv.mat','chi2_sims_rdc_p_mins')

chi2_sims_rdc_p_mins_p = chi2_sims_rdc_p_mins;

load('iaerr_perts/chi2_sims_rdc_p_mins_AHv.mat','chi2_sims_rdc_p_mins')

chi2_sims_rdc_p_mins_r = chi2_sims_rdc_p_mins;

clear chi2_sims_rdc_p_mins

age_data = [0.9472566667 2.0108057143].*1e3;

age_err = [0.0218016667 0.0152742857].*1e3;

% 2. Plot late Amazonian volcanic unit

fig1 = figure(1);

hold on

set(gca, 'XScale', 'log')

x1 = [21 age_data(1) age_data(1) 21];

y1 = [obl_data(1)-obl_errlow(1) obl_data(1)-obl_errlow(1)...
       obl_data(1)+obl_errhigh(1) obl_data(1)+obl_errhigh(1)];

y1_pert = [obl_pert_data(1)-obl_pert_errlow(1)...
            obl_pert_data(1)-obl_pert_errlow(1)...
            obl_pert_data(1)+obl_pert_errhigh(1)...
            obl_pert_data(1)+obl_pert_errhigh(1)];

x1e = [age_data(1)-age_err(1) age_data(1)+age_err(1)...
        age_data(1)+age_err(1) age_data(1)-age_err(1)];

patch(x1e,y1,'white','EdgeColor','#8D6135','LineStyle','--')

```

```

patch(x1e,y1_pert,'white','EdgeColor','#74C1E4','LineStyle','--')

for i = 1:1000

    patchline([21 age_data(1)],[chi2_sims_rdc_p_mins_p(i)...
        chi2_sims_rdc_p_mins_p(i)],...
        'edgecolor','#74C1E4','linewidth',5,'edgealpha',0.01)

end

plot([21 age_data(1)],[obl_data(1) obl_data(1)],'Color','#8D6135',...
    'LineWidth',2)

plot([21 age_data(1)],[obl_pert_data(1) obl_pert_data(1)],'Color',...
    '#74C1E4','LineWidth',2)

plot([21 age_data(1)],[obl_data(1)+obl_errhigh(1)...
    obl_data(1)+obl_errhigh(1)],'Color','#8D6135',...
    'LineStyle','--','LineWidth',0.75)

plot([21 age_data(1)],[obl_data(1)-obl_errlow(1)...
    obl_data(1)-obl_errlow(1)],'Color','#8D6135',...
    'LineStyle','--','LineWidth',0.75)

plot([21 age_data(1)],[obl_pert_data(1)+obl_pert_errhigh(1)...
    obl_pert_data(1)+obl_pert_errhigh(1)],'Color',...
    '#74C1E4','LineStyle','--','LineWidth',0.75)

plot([21 age_data(1)],[obl_pert_data(1)-obl_pert_errlow(1)...
    obl_pert_data(1)-obl_pert_errlow(1)],'Color',...
    '#74C1E4','LineStyle','--','LineWidth',0.75)

```

```

plot([age_data(1) age_data(1)], [obl_data(1)+obl_errhigh(1)...
    obl_data(1)-obl_errlow(1)], 'Color', ...
    '#8D6135')

% 3. Plot Amazonian-Hesperian volcanic unit

x2 = [21 age_data(2) age_data(2) 21];
y2 = [obl_data(2)-obl_errlow(2) obl_data(2)-obl_errlow(2)...
    obl_data(2)+obl_errhigh(2) obl_data(2)+obl_errhigh(2)];
y2_pert = [obl_pert_data(2)-obl_pert_errlow(2)...
    obl_pert_data(2)-obl_pert_errlow(2)...
    obl_pert_data(2)+obl_pert_errhigh(2)...
    obl_pert_data(2)+obl_pert_errhigh(2)];

x2e = [age_data(2)-age_err(2) age_data(2)+age_err(2)...
    age_data(2)+age_err(2) age_data(2)-age_err(2)];
patch(x2e,y2, 'white', 'EdgeColor', '#8D6135', 'LineStyle', '--')

patch(x2e,y2_pert, 'white', 'EdgeColor', '#74C1E4', 'LineStyle', '--')

for i = 1:1000
    patchline([21 age_data(2)], [chi2_sims_rdc_p_mins_r(i)...
        chi2_sims_rdc_p_mins_r(i)], ...
        'edgecolor', '#74C1E4', 'linewidth', 5, 'edgealpha', 0.01)
end

```

```

plot([21 age_data(2)],[obl_data(2) obl_data(2)],'Color','#8D6135',...
    'LineWidth',2)

plot([21 age_data(2)],[obl_pert_data(2) obl_pert_data(2)],'Color',...
    '#74C1E4','LineWidth',2)

plot([21 age_data(2)],[obl_data(2)+obl_errhigh(2)...
    obl_data(2)+obl_errhigh(2)],'Color','#8D6135',...
    'LineStyle','--','LineWidth',0.75)

plot([21 age_data(2)],[obl_data(2)-obl_errlow(2)...
    obl_data(2)-obl_errlow(2)],'Color','#8D6135',...
    'LineStyle','--','LineWidth',0.75)

plot([21 age_data(2)],[obl_pert_data(2)+obl_pert_errhigh(2)...
    obl_pert_data(2)+obl_pert_errhigh(2)],'Color',...
    '#74C1E4','LineStyle','--','LineWidth',0.75)

plot([21 age_data(2)],[obl_pert_data(2)-obl_pert_errlow(2)...
    obl_pert_data(2)-obl_pert_errlow(2)],'Color',...
    '#74C1E4','LineStyle','--','LineWidth',0.75)

plot([age_data(2) age_data(2)],[obl_data(2)+obl_errhigh(2)...
    obl_data(2)-obl_errlow(2)],'Color',...
    '#8D6135')

% 4. Laskar numerical reverse integration

load('laskar/laskar_chaotic1.mat')

patchline(laskar1(:,1).*1e-3,rad2deg(laskar1(:,2)),'linestyle','--',...

```

```

'edgecolor',[0.9290 0.6940 0.1250],'linewidth',0.5, ...
'edgealpha',0.01);

load('laskar/laskar_chaotic2.mat')

patchline(laskar2(:,1).*-1e-3,rad2deg(laskar2(:,2)), 'linestyle','--',...
'edgecolor',[0.4940 0.1840 0.5560], 'linewidth',0.5, ...
'edgealpha',0.01);

load('laskar/laskar_chaotic3.mat')

patchline(laskar3(:,1).*-1e-3,rad2deg(laskar3(:,2)), 'linestyle','--',...
'edgecolor',[0.4660 0.6740 0.1880], 'linewidth',0.5, ...
'edgealpha',0.01);

load('laskar/laskar_chaotic4.mat')

patchline(laskar4(:,1).*-1e-3,rad2deg(laskar4(:,2)), 'linestyle','--',...
'edgecolor',[0.8500 0.3250 0.0980], 'linewidth',0.5, ...
'edgealpha',0.01);

load('laskar/laskar_chaotic5.mat')

patchline(laskar5(:,1).*-1e-3,rad2deg(laskar5(:,2)), 'linestyle','--',...
'edgecolor',[0.6350 0.0780 0.1840], 'linewidth',0.5, ...
'edgealpha',0.01);

load('laskar/laskar_nonchaotic.mat')

plot(laskar(:,1).*-1e-3,rad2deg(laskar(:,2)), 'Color',...
[0.6350 0.0780 0.1840], 'LineWidth',1)
scatter(1e-1,25.1,120,'x','LineWidth',1,'MarkerEdgeColor','k')

% 5. Processing

xt = [13 12 3e-1];

```


A.8 hu_08_perturb_data_iaerr.m

```

%% **** STEP 08 ****
% Create inter-analyst-perturbed crater azimuth arrays.

%
% ****
e_crit = 1.05;
N = 1000; % Number of instances of inter-analyst perturbation

%
% Load crater data and inter-analyst perturbation options
for mode = 1:2 % 1 = lAv; 2 = AHv

```

```

if mode == 1
    load(sprintf('craters_obs/lAv%.2f.mat',e_crit))
elseif mode == 2
    load(sprintf('craters_obs/AHv%.2f.mat',e_crit))
end

load(sprintf("iaerr_perts/iaerr_Kite%.2f.mat",e_crit))
kite = azimuth_diff;
load(sprintf("iaerr_perts/iaerr_Holo%.2f.mat",e_crit))
holo = azimuth_diff;
azimuth_diff = cat(1,kite,holo);

cratdata = a(:,2);
clear('a')

% Set random seed
rng('default');
rng(1);

% Create perturbation array
l = length(cratdata);
perts = reshape(datasample(azimuth_diff,N*l),[l,N]);

% Perturb
cratdata_p = zeros(l,N);
for i = 1:N

```

```

cratdata_p(:,i) = cratdata + perts(:,i);

% Refold azimuths above 90° and below 0°

for j = 1:l

    if (cratdata_p(j,i) > 90 || cratdata_p(j,i) < 0)

        cratdata_p(j,i) = 90 - mod(cratdata_p(j,i),90);

    end

end

if mode == 1

    fname = sprintf('iaerr_perts/lAv%.2f_pert%d.mat',e_crit,N);

    save(fname,'cratdata_p')

elseif mode == 2

    fname = sprintf('iaerr_perts/AHv%.2f_pert%d.mat',e_crit,N);

    save(fname,'cratdata_p')

end

end

```

877

A.9 hu_09_get_mismatch_var_ecrit.m

```

%% ***** STEP 09 *****
% Redo step 6 (with simplifications) for various e_crit values, i.e., 1.00,
% 1.05, 1.10, and 1.15.

%
% ***** *****

```

James Hu, 2022

```

% 1. Load the appropriate crater data and latitude-normalized obliquity
% predictions.

scenario = 2; % 1 = constant obliquity;
                % 2 = Gaussian variation around mean obliquity

if scenario == 2

    sigma = 5.0326; % Standard deviation from Laskar 2004, past 2.5 Ma:
                      % load('laskar/laskar_nonchaotic.mat')
                      % rad2deg(std(laskar(1:2501,2)))

end

for mode = 1:2 % 1 = lAv; 2 = AHv

    if mode == 1

        load('craters_obs/lAv1.00.mat')

        a100 = a;

        load('craters_obs/lAv1.05.mat')

        a105 = a;

        load('craters_obs/lAv1.10.mat')

        a110 = a;

        load('craters_obs/lAv1.15.mat')

        a115 = a;

        clear('a')

        load('forward_model/obpreds4_norm_lAv1.00.mat','orientationdata')

        orientationdata100 = orientationdata;

        load('forward_model/obpreds4_norm_lAv1.05.mat','orientationdata')

        orientationdata105 = orientationdata;

        load('forward_model/obpreds4_norm_lAv1.10.mat','orientationdata')

```

```

orientationdata110 = orientationdata;

load('forward_model/obpreds4_norm_lAv1.15.mat','orientationdata')

orientationdata115 = orientationdata;

clear('orientationdata')

elseif mode == 2

    load('craters_obs/AHv1.00.mat')

    a100 = a;

    load('craters_obs/AHv1.05.mat')

    a105 = a;

    load('craters_obs/AHv1.10.mat')

    a110 = a;

    load('craters_obs/AHv1.15.mat')

    a115 = a;

    clear('a')

    load('forward_model/obpreds4_norm_AHv1.00.mat','orientationdata')

    orientationdata100 = orientationdata;

    load('forward_model/obpreds4_norm_AHv1.05.mat','orientationdata')

    orientationdata105 = orientationdata;

    load('forward_model/obpreds4_norm_AHv1.10.mat','orientationdata')

    orientationdata110 = orientationdata;

    load('forward_model/obpreds4_norm_AHv1.15.mat','orientationdata')

    orientationdata115 = orientationdata;

    clear('orientationdata')

end

cratdata100 = a100(:,2);

```

```

cratdata105 = a105(:,2);
cratdata110 = a110(:,2);
cratdata115 = a115(:,2);

% 2. Take the actual crater orientations and construct crude
% probability distribution function (histogram)

bin_centers = 5:10:85;
num_bins = width(bin_centers);

[N100,X] = hist(cratdata100,bin_centers); % Raw frequencies
[N105,X] = hist(cratdata105,bin_centers);
[N110,X] = hist(cratdata110,bin_centers);
[N115,X] = hist(cratdata115,bin_centers);

num_crats100 = height(cratdata100);
num_crats105 = height(cratdata105);
num_crats110 = height(cratdata110);
num_crats115 = height(cratdata115);

N_norm100 = N100 / num_crats100 / num_bins; % Normalized distribution
N_norm105 = N105 / num_crats105 / num_bins;
N_norm110 = N110 / num_crats110 / num_bins;
N_norm115 = N115 / num_crats115 / num_bins;

%% Compare the PDFs of the actual and simulated crater orientations

% 3. Calculate the standard error on the actual crater probability
% distribution function; plot with error bars

fig1 = figure('color',[1 1 1]);

```

```

subplot(2,1,mode)

hold on

plot(X,N_norm100,'Color','#74C1E4','LineWidth',1.5,'LineStyle',':');

E105 = sqrt(N105) / num_crats105 / num_bins;

errorbar(X,N_norm105,E105,'Color','#8D6135','LineWidth',1.5)

plot(X,N_norm110,'Color','#74C1E4','LineWidth',1.5,'LineStyle','-.');

plot(X,N_norm115,'Color','#74C1E4','LineWidth',1.5,'LineStyle','--');

% 4. Take the simulated crater orientation data and construct crude
% probability distribution functions; plot

sims100 = zeros(91,num_bins);

sims105 = zeros(91,num_bins);

sims110 = zeros(91,num_bins);

sims115 = zeros(91,num_bins);

num_simcrats = height(orientationdata100); % This is the same for all e_crits

for i = 0:1:90 % Loop through all obliquity scenarios

    if scenario == 1

        odata100 = orientationdata100(:,i+1);

        odata105 = orientationdata105(:,i+1);

        odata110 = orientationdata110(:,i+1);

        odata115 = orientationdata115(:,i+1);

    elseif scenario == 2

        odata100 = hu_06b_gaussamp(orientationdata100,i,sigma);

        odata105 = hu_06b_gaussamp(orientationdata105,i,sigma);

    end
end

```

```

odata110 = hu_06b_gaussamp(orientationdata110,i,sigma);
odata115 = hu_06b_gaussamp(orientationdata115,i,sigma);

end

f100 = hist(odata100,bin_centers) / num_simcrats / num_bins;
sims100(i+1,:) = f100;

f105 = hist(odata100,bin_centers) / num_simcrats / num_bins;
sims105(i+1,:) = f105;

f110 = hist(odata100,bin_centers) / num_simcrats / num_bins;
sims110(i+1,:) = f110;

f115 = hist(odata100,bin_centers) / num_simcrats / num_bins;
sims115(i+1,:) = f115;

end

%% Conduct 91 chi-squared tests to determine best-match constant obliquity

% 5. Calculate reduced chi-squared values for each obliquity

chi2_sims100 = hu_06a_chi2test(sims100'*num_crats100*num_bins,N100');
chi2_sims105 = hu_06a_chi2test(sims105'*num_crats105*num_bins,N105');
chi2_sims110 = hu_06a_chi2test(sims110'*num_crats110*num_bins,N110');
chi2_sims115 = hu_06a_chi2test(sims115'*num_crats115*num_bins,N115');

chi2_sims_rdc100 = chi2_sims100 / (num_bins-1);
chi2_sims_rdc105 = chi2_sims105 / (num_bins-1);
chi2_sims_rdc110 = chi2_sims110 / (num_bins-1);

```

```

chi2_sims_rdc115 = chi2_sims115 / (num_bins-1);

%% 6. Plot

fig2 = figure('color',[1 1 1]);
hold on
ylim([0 25])
plot(0:90,chi2_sims_rdc100,'LineWidth',1.5,'Color','#74C1E4',...
'LineStyle',':');
plot(0:90,chi2_sims_rdc105,'LineWidth',1.5,'Color','#8D6135');
plot(0:90,chi2_sims_rdc110,'LineWidth',1.5,'Color','#74C1E4',...
'LineStyle','-.');
plot(0:90,chi2_sims_rdc115,'LineWidth',1.5,'Color','#74C1E4',...
'LineStyle','--');

% 7. Draw lines on plot - commented out; use to find uncertainty
[yMin_rdc,xIndex_rdc] = min(chi2_sims_rdc100); % Observed
xline(xIndex_rdc-1,'Color','#8D6135')
y_uncert_rdc = yMin_rdc + 1/(num_bins-1);
yline(y_uncert_rdc,'Color','#8D6135')
y_uncert_rdc_arr = y_uncert_rdc + zeros(1,91);
[xIndex_uncert_rdc,~] = intersections(0:90,chi2_sims_rdc100,0:90, ...
y_uncert_rdc_arr);
xline([min(xIndex_uncert_rdc) max(xIndex_uncert_rdc)],'Color',...
'#8D6135') % Uncertainty (x)

% 8. Post-processing

```

```

clearvars -except mode scenario sigma fig*

if mode == 1
    fig11 = fig1;
    fig21 = fig2;
elseif mode == 2
    fig12 = fig1;
    fig22 = fig2;
end

clear fig1 fig2
end

%% Tile plots together

% 9. Figure 3.1

fig1 = figure;
t1 = tiledlayout(1,2,'TileSpacing','compact');

fig1a = nexttile;
copyobj(allchild(get(fig11,'CurrentAxes')),fig1a)
title('(a)')
xlim([0 90])
ylim([0.006 0.03])

fig1b = nexttile;

```

```

copyobj(allchild(get(fig12, 'CurrentAxes')),fig1b)

title('(b)')

xlim([0 90])

ylim([0.006 0.03])

ylabel(t1, 'Probability density')

xlabel(t1, 'Azimuth (° from due north)')

l1 = legend('1.00','1.05','1.10','1.15');

l1.Orientation = 'vertical';

fig1.PaperUnits = 'centimeters';

fig1.PaperPosition = [0 0 24 16];

print(fig1,'output/fig4_2','-dpng','-r500')

```

% 10. Figure 3.2

```

fig2 = figure;

t2 = tiledlayout(1,2,'TileSpacing','compact');

fig2a = nexttile;

copyobj(allchild(get(fig21, 'CurrentAxes')),fig2a)

title('(a)')

xlim([0 90])

ylim([0 30])

set(gca,'Ydir','reverse')

fig2b = nexttile;

```

```

copyobj(allchild(get(fig22, 'CurrentAxes')),fig2b)

title(' (b)')

xlim([0 90])

ylim([0 30])

set(gca, 'Ydir', 'reverse')

ylabel(t2, 'Mismatch (reduced \chi^2 statistic)')

xlabel(t2, 'Obliquity (°)')

12 = legend('1.00','1.05','1.10','1.15');

12.Orientation = 'vertical';

fig2.PaperUnits = 'centimeters';

fig2.PaperPosition = [0 0 24 16];

print(fig2,'output/fig4_3','-dpng',' -r500')

```

878

A.10 hu_10_plot_distributions.m

```
%% ***** STEP 10 *****
% Plot distributions of crater latitudes, azimuths, and ellipticities.
%
% *****

e_crit = 1.05;

% Latitude distribution

load('forward_model/obpreds4.mat','orientationdata','latdata','diamdata')
```

```

fig1 = figure;
t = tiledlayout(1,2,'TileSpacing','compact');

nexttile
load(sprintf('craters_obs/lAv%.2f.mat',e_crit))
folded_lats = abs(a(:,1));
lAv = a;
hist(folded_lats,2.5:5:87.5)
h = findobj(gca,'Type','patch');
h.FaceColor = '#74C1E4';
xlim([0 90])
ylim([0 300])
title('(a)')

nexttile
load(sprintf('craters_obs/AHv%.2f.mat',e_crit))
folded_lats = abs(a(:,1));
AHv = a;
hist(folded_lats,2.5:5:87.5)
h = findobj(gca,'Type','patch');
h.FaceColor = '#74C1E4';
xlim([0 90])
ylim([0 300])
title('(b)')

```

```

ylabel(t, 'Frequency')

xlabel(t, 'Latitude (°)')

fig1.PaperUnits = 'centimeters';
fig1.PaperPosition = [0 0 24 16];
print(fig1,'output/fig4_1',' -dpng ',' -r500 ')

% Azimuth distribution
a = cat(1,lAv,AHv);
azimuths = a(:,2);

fig2 = figure;

hist(azimuths,2.5:5:87.5)
h = findobj(gca,'Type','patch');
h.FaceColor = '#74C1E4';

ylabel('Frequency')
xlabel('Azimuth (°)')
xlim([0 90])

fig2.PaperUnits = 'centimeters';
fig2.PaperPosition = [0 0 24 16];
print(fig2,'output/fig4_4',' -dpng ',' -r500 ')

% Ellipticity distribution

```

```

load('craters_obs/lAv1.00.mat')
lAv100 = a;
load('craters_obs/AHv1.00.mat')
AHv100 = a;
a = cat(1,lAv100,AHv100);
ellips = a(:,4);
clear('a')

fig2 = figure;

hist(ellips,1.0125:0.025:1.9875)
h = findobj(gca,'Type','patch');
h.FaceColor = '#74C1E4';

ylabel('Frequency')
xlabel('Ellipticity')
xlim([1 2])

fig2.PaperUnits = 'centimeters';
fig2.PaperPosition = [0 0 24 16];
print(fig2,'output/fig2_4','-dpng','-r500')

```